Understanding the White-Emitting $CaMoO_4$ Co-Doped Eu^{3+}, Tb^{3+} and Tm^{3+} Phosphor Through Experiment and Computation

R.L. Tranquilin[a], L.X. Lovisa[a], C.R.R. Almeida[a], C.A. Paskocimas[a], M.S. Li[b], M. C. Oliveira[a,c], L. Gracia[c,#], J.Andres[c], E. Longo[d,*], F.V. Motta[a], M.R.D. Bomio[a]

[a]LSQM – Laboratory of Chemical Synthesis of Materials – Department of Materials Engineering, Federal University of Rio Grande do Norte, P.O. Box 1524, 59078-900, Natal, RN, Brazil.

[b] IFSC, USP, Av. Trabalhador São Carlense, 400, CEP 13566-590, São Carlos, SP, Brazil

[c]Departament de Química Física i Analítica, Universitat Jaume I, 12071 Castelló de la Plana, Spain

[#] Permanent address: Department of Physical Chemistry, Universitat de València, 46100 Burjassot, Spain

[d] CDMF-LIEC, UFSCar, P.O. Box 676, 13565-905 São Carlos, SP, Brazil

Abstract

In this article, the synthesis by means spray pyrolysis method, of the $CaMoO_4$ and rare earth cation (RE^{3+})-doped $CaMoO_4$:xRE^{3+} (RE^{3+} = Eu^{3+}, Tb^{3+}, and Tm^{3+}; and x= 1%, 2%, and 4% mol) compounds is presented. The as-synthesized samples were characterized using x-ray diffraction (XRD), Rietveld refinement, field emission scanning electron microscopy (FE-SEM), Raman spectroscopy, and photoluminescence (PL) spectroscopy. To complement and rationalize the experimental results, first principle calculation, at density functional theory level, have been performed to analyze the band structure and density of states. In addition, a theoretical method based on the calculations of surface energies and Wulff construction was applied to obtain the morphology transformation of the $CaMoO_4$ and $CaMoO_4$:RE^{3+} microstructures. The experimental morphologies can be observed in the FE-SEM images. The PL behavior of the co-doped samples exhibited well-defined bands in the visible region. The samples with 2% and 4% of RE^{3+} released white emission according to the chromaticity coordinates (0.34, 0.34) and (0.34, 0.33), respectively. Present results provide not only a deep understanding of the structure–property relationships of $CaMoO_4$-based phosphor, but also can be employed as a guideline for the design of the electronic structure of the materials and the fabrication of photo-functional materials with optimal properties, which allows for the modeling of new phosphors for applications in solid-state lighting.

* Corresponding authors

E-mail address: elson.liec@gmail.com (E. Longo)

mauricio.bomio@ct.ufrn.br (M.R.D. Bomio)

1. INTRODUCTION

Designing new materials for solid state lighting and understanding the various intricacies involved for designing them such as defects, energy transfer and concentration quenching is very important. Such materials will be highly beneficial in optical devices energy and health industry. The current challenge is to fabricate a material that meets the requirements (thermal and chemical stability, color purity, and emitted color productivity) for its use. White light emitting diodes (WLEDs) consist of blue LED chips associated with YAG:Ce^{3+} (yellow emission) phosphor [1], which is considered as an important source in the display technology. However, there are several limiting factors with respect to its use, which correspond to a low color rendering index (CRI) due to the scarcity of red light in the YAG:Ce^{3+} emission, in addition to the low color stability associated with the changes in the transmission voltage. To enhance the CRI, WLEDs are fabricated from a single-phase matrix that efficiently hosts rare earth type dopants, which exhibit different types of emission in the visible region[2]. Notable characteristics of tri-doped matches with rare earth are their luminous efficiency, excellent CRI, adjustable temperature, and purity with respect to chromaticity coordinates[3]. According to Park et al.[4], the energy transfer (matrix → dopant) coupled with the adjusted concentrations of activators and sensitizers can be worked up to obtain white light-emitting phosphors.

Alkali-earth molybdates $MMoO_4$ (M=Ca, Sr, Ba) include a wide range of scientifically and technologically significant compounds. These materials are chemically designed and further synthesized using different methods based on the final objective [5-9]. In particular, molybdates phosphors were implemented in optical applications [10-11] and evaluated extensively over the past century as a scintillating medium and electro-optical devices, given their broad and intense absorption bands due to the charge transfer (CT) from oxygen to the metal in the near-ultraviolet (UV) region [12-16]. Among molybdates, $CaMoO_4$ is considered an outstanding matrix material for the synthesis of highly applicable luminescent materials due to its excellent physical and chemical properties[17-24]. Moreover, $CaMoO_4$ exhibits a tetragonal structure and space group $I4_1/a$ [25]. In the scheelite structure, the Mo cations are bonded to four oxygens, which form the tetrahedral [MoO_4] clusters; whereas the Ca cations are coordinated to eight oxygen anions, which form the dodecahedron [CaO_8] clusters[10, 26] and can be described as a layered arrangement composed of non-interconnected [MoO_4] and [CaO_8] clusters that form chains parallel to $[1\bar{1}0]$ with a shared edge [27]. In addition, $CaMoO_4$ based materials are also important materials that can be used in various applications such as photoluminescence (PL) and microwave applications [28-29], scintillators

[30-31], photocatalysis[7], and the emission of light in the blue-green region of the electromagnetic spectrum after excitation with UV light[32]. In particular, when cations are introduced into the structure, structural distortions of the tetrahedron and dodecahedron chains occur[33]. Structural disorders in crystals of inorganic materials are present where two or more types of cations or anions statistically occupy the same lattice site.

Inorganic materials doped with RE^{3+} (RE^{3+}: rare earth**)** have structural disorders with a distribution of local cationic environments around the doping sites, which deviate from that of the ideal crystallographic positions. These materials attracted significant attention due to their novel structural characteristics and potential applications in various fields[34-35]. In particular, RE^{3+} are added to the host matrices to enhance the luminescent properties[19, 36]. PL spectroscopy is a very efficient tool for the evaluation of the order-disorder effects in semiconductors, which leads to a better understanding of the structural changes that take place in materials. In particular, the scheelite-type molybdates are interesting materials [37-38] due to their scientific significance, especially with respect to technological applications[39]. The electronic and optical properties of the luminescent materials are significantly influenced by intrinsic and extrinsic defects[40]. These dopant elements favor luminescent properties due to their characteristics and well-defined transitions in the visible range. Moreover, due to their excellent spectroscopic properties, several applications that involve the use of RE^{3+}cations have been reported[33, 41-43].

Furthermore, $CaMoO_4$ exhibits a broad blue-green luminescence emission peak in the range of 350–650 nm with a peak maximum at approximately 500 nm, which can be tuned as a function of the particle size and the presence of oxygen vacancies in the lattice[44]. In theory, this behavior can be attributed to the electron–hole recombination process after excitation through the band gap of the charge transfer from the 2p orbital of the O anions to the 4d orbitals of the Mo cations in the $(MoO_4)^{2-}$ complex tetrahedron[45]. However, the emission band is very broad, and it is difficult to tune the color, particularly for lighting and display applications. On the other hand, the RE^{3+} cations have poor absorption cross-sections due to the forbidden nature of the f–f transitions with poor luminescence emission[46]. For the PL emissions, the electron transitions in the 4f and 4d orbitals of the RE^{3+} and Mo^{6+}cations, respectively, should be considered. Given that the energy level of the 4f orbital is lower than that of the 4d orbital, the possible electron transitions are 4f–4f or 4f–4d. Due to the orbital radius, the 4f orbital is shielded by the 4s and 4p orbitals; however, the 4d orbital is exposed. Therefore, for RE^{3+}cations, the 4f–4f transitions are not influenced by the surroundings, and they exhibit a constant energy gap; whereas the 4f–4d transitions are influenced by the

structure, and they exhibit a broad spectrum. The intense and abrupt 4f–4f transitions are a result of the protected external environment due to the 5s and 5p electrons. In addition, according to the Laporte rule, the 4f–4f transition is prohibited; thus, the luminescence based on these transitions is weaker than that of the 4f–4d transitions. Hence, by combining 4f–4f transitions, which exhibit intrinsic luminescence, with 4f–4d transitions, which vary depending on the structure; orange-yellow phosphors with a variety of elements can be developed. This leads to an improvement in the light quality and color reproducibility[47-48]. Consequently, RE^{3+} doped materials can be used in various applications such as field emitting displays and LEDs[49-54].

$CaMoO_4$ has good chemical and heat stabilities, and itis considered an excellent matrix material. Its luminescence properties can be enhanced when doped with the RE^{3+} cations[19, 55-57], e.g., RE^{3+}= Eu^{3+}, Tb^{3+}, and Tm^{3+}. Moreover, structural disorders occur when RE^{3+}cations occupy the crystallographic sites of $CaMoO_4$, and when an energy transfer process takes place from the host/sensitizer to the excited state of the activator by a non-radiative energy transfer mechanism[58]. In addition, both processes render a high population of photons in the excited level/levels of RE^{3+} with concomitant enhanced emissions of RE^{3+} [59]. Different synthesis methods have been employed to enrich the luminescent efficiency of the as-prepared luminescent materials ions-doped molybdates which include the $CaMoO_4$ material [13, 22, 32, 60-65] The abovementioned synthesis methods include the Czochralski method[18]; chemical precipitation method[66-67]; citrate-gel method[68]; hydrothermal method[69-71]; polyol process [72], supersaturated recrystallization process[73]; solid-state reaction;[12] sol-gel process[13], wherein the quantum efficiency of the material is 20% higher than that fabricated using a solid state reaction sonochemical method[74]; and microwave reaction[27, 75].

The spray pyrolysis method is used for the synthesis of aluminate phosphors and LED phosphor applications, as it offers a high efficiency for the formation of non-agglomerated and fine particles with well-defined morphologies, which can increase the brightness and resolution[76]. The spray pyrolysis method is also a promising alternative for the synthesis of rare earth doped molybdates, as it i) does not require a high-vacuum environment, and ii) it can be carried out using simple instrumentation at a low cost[77]. The pyrolysis spray method presents as a synthesis route in which nanoparticles in suspension can be easily obtained and manipulated to realize specific morphologies. What makes aerosol science and technology enabled for areas of high performance in nanotechnology[78]. A major objective of the pyrolysis spray method is to present a single process step, and the realization of a high productivity and high control of the properties of the particles produced[79]. The

abovementioned characteristics of the method are of great significance with respect to applications in various industrial fields. The control of the size and morphology of the particles produced is mainly determined by the type of aerosol generator[80]. Consequently, atomization is a major focus of this work. The atomization ultrasound, which was used in the experimental procedure, produces droplets with a fairly uniform size distribution. From recent studies in which the spray pyrolysis technique was used, it was reported that it can be implemented for the production of various powder materials such as inorganic oxides, metals oxides, and nanoparticle oxides, among other compounds[28-29, 81-82].

In this work, an effort has been taken in that direction and, for the first time, the synthesis of $CaMoO_4$ and $CaMoO_4$-doped rare earth RE^{3+} (RE^{3+}= Eu^{3+}, Tb^{3+}, and Tm^{3+}), $CaMoO_4$: x RE^{3+} composites at different percentages, x=1% (Eu^{3+}(1%), Tb^{3+}(1%), and Tm^{3+}(1%)), x=2% (Eu^{3+}(2%), Tb^{3+}(2%), and Tm^{3+}(2%)), and x=4% (Eu^{3+}(4%), Tb^{3+}(4%), and Tm^{3+}(4%)), via the spray pyrolysis method without the addition of any surfactants and templates is reported. The as-synthesized samples were characterized using x-ray diffraction (XRD), field emission scanning electron microscopy (FE-SEM), Raman spectroscopy, and PL spectroscopy. The color coordinates, color temperature, and color rendering index (CRI) were also investigated. The materials obtained were tested for their applicability as white light emitters. In addition, first-principles quantum-mechanical calculations based on the density functional theory (DFT) are performed to complement and rationalize the experimental results; in particular the local structure, morphology, band gap, and electronic and optical properties of the pure $CaMoO_4$ and $CaMoO_4$:RE^{3+}composites. A theoretical method, based on the calculations of surface energies and Wulff construction, was applied to study the morphology transformations. From an analysis of the results of the characterization experiment and first-principles calculations, the nature of the mechanism for the luminescence emissions were revealed.

2. EXPERIMENTAL SECTION

2.1. Materials

Molybdic acid (H_2MoO_4, 85%, Alfa Aesar), calcium nitrate ($Ca(NO_3)_2.4H_2O$, 99%, Alfa Aesar), nitric acid (HNO_3-synth, 99.9%) europium oxide (Eu_2O_3, 99%, Aldrich), terbium nitrate pentahydrate ($Tb(NO_3).5H_2O$, 99% Aldrich 99.9%), thulium oxide (Tm_2O_3,

99%, Aldrich), and distilled water were used as-received for the preparation of the $CaMoO_4:RE^{3+}$microstructures.

2.2. Preparation of $CaMoO_4:RE^{3+}$

Calcium molybdate powders ($CaMoO_4$) were processed using the spray pyrolysis method with the addition of europium (Eu^{3+}), thulium (Tm^{3+}), and terbium (Tb^{3+}) rare earths. The experimental procedure was conducted as described. The precursors of calcium nitrate and the molybdic acid were dissolved separately in a beaker that contained 100 ml of deionized water. The resulting solution was then added to a beaker, and then homogenized at approximately at 60°C. Under constant stirring and a stabilized temperature (60°C), Eu^{3+} (europium), Tb^{3+} (terbium), and Tm^{3+} (thulium) were added to the reaction in the proportions presented in Table 1. For the Eu^{3+} and Tm^{3+} dopants, it was necessary to dissolve the oxides Tm_2O_3 and Eu_2O_3 in approximately 10 mL of nitric acid HNO_3 under stirring at 60°C to form the respective nitrates. In this manner, all the dopants in the reaction could be solubilized. The reagents were stoichiometrically weighed and added to the calcium molybdate solution. The solution remained under agitation and was temperature-controlled for approximately 30 min.

Table 1.

Figure 1 presents a schematic of the spray pyrolysis system. The droplet generator comprised an ultrasonic nebulizer. The laminar flow aerosol reactor used in the present study was a quartz tube with an inner diameter of 37 mm and length of 1.86 m, which was inserted into a horizontal electric furnace. The precursor solution was atomized at a frequency of 2.4 MHz using the ultrasonic nebulizer. The sprayed droplets were carried to the reactor, heated by an electric furnace at 600°C in air, and converted into solid oxide particles within the laminar-flow aerosol reactor. The resulting particles were collected at the reactor exit using an electrostatic precipitator. The overall flow rate of the air used as a carrier gas was 2 L min^{-1}. The residence time of the $CaMoO_4:RE^{3+}$solution in the reactor is a function of the drag gas flow and the reactor area volume according to Equation 1[83].

$$T = \frac{R}{60Q} \quad (1)$$

Where T is the residence time (s), R is the gas flow rate (L min^{-1}), and V is the reactor volume (L). The reactor volume was 1.61 L, and the air flow rate was 2 L min^{-1}. From this relationship, the mean time of synthesis was calculated as approximately 48 s.

Figure 1 presents a schematic that includes all the stages of the synthesis and growth of the nanocrystal $CaMoO_4$ and $CaMoO_4:RE^{3+}$ microstructures obtained using the spray pyrolysis method. At Stage 1, the thermal decomposition occurs directly at the nucleation sites, which promotes the crystallization kinetics of the initial crystals. Due to the free rotation of the primary crystals, random collisions and re-arrangements of the crystals can occur through movement at this stage, which comprises Stages 2 and 3, and the nanocrystals are effectively generated. At Stage 4, the nanocrystals tend to undergo self-assembly, possibly via Van der Waals interactions[46], to achieve the minimum energy per volume ratio[84]. Favoring the growth kinetics of nanocrystals, the thermal decomposition can promote the heterogeneous nucleation and aggregation of the $CaMoO_4$ and $CaMoO_4:RE^{3+}$ nanocrystals. The growth promotion occurs at Stage 5, which is responsible for the formation and growth of the aggregated $CaMoO_4$ or $CaMoO_4:RE^{3+}$ nanocrystals. The high drying temperature can generate a temperature gradient between the inner surface of the crystals and their interior, which leads to thermal stress on the crystals.

Figure 1.

2.3. Characterization of the $CaMoO_4:RE^{3+}$microstructures

The $CaMoO_4:RE^{3+}$ microstructures were structurally characterized by XRD using a Shimadzu XRD 7000 instrument with Cu-Kα radiation (λ = 1.5406 Å) at 2θ = 10–80º and a scanning rate of $0.02^{o}s^{-1}$. Micro-Raman spectroscopy measurements were carried out using a T-64000 spectrometer (JobinYvon, France) with a triple monochromator coupled to a charge couple detector (CCD). The spectra were obtained using an argon ion laser with a wavelength of 514.5 nm and a maximum output power of 8 mW. The morphologies were evaluated using field emission-scanning electron microscopy (FE-SEM) (Carl Zeiss, Supra 35- VP Model, Germany). The ultraviolet–visible (UV-vis) diffuse reflectance spectrum was measured at room temperature using a UV-vis spectrometer. The PL spectra were obtained using an Ash Monospec 27 monochromator (Thermal Jarrel, U.S.A.) and a R4446 photomultiplier

(Hamamatsu Photonics, U.S.A.). The 350 nm beam of a krypton ion laser (Coherent Innova 90 K) was used as the excitation source with a maximum output power of 200 mW. All the measurements were carried out at room temperature.

In the synthesis of $CaMoO_4$ and $CaMoO_4$: RE^{3+}, the quantities of the regents used were weighted stoichiometrically according to the values presented in Table 1. To verify the chemical composition of the samples, a chemical analysis of the material was carried out from energy-dispersive X-ray spectroscopy (EDS).

3. COMPUTATIONAL DETAILS

The bulk of the $CaMoO_4$ structure was doped with 12.5% mol of Eu^{3+}, Tb^{3+}, and Tm^{3+}. Simulations were conducted using quantum-mechanical calculations based on the DFT framework at the B3LYP hybrid functional level[85-86] in the CRYSTAL17 computer code[87]. This method was successfully employed, as reported in several studies conducted on the bulk, electronic, and structural properties of molybdate[88-90], tungstate[91-92], vanadate[93-94] and perovskite[95] based materials, in addition to Ag_2CrO_4[96].

The atomic centers were described using standard all-electron basis sets (6-31G* basis set) for the O and Ca atoms; whereas the Mo, Eu, Tb, and Tm atoms were described by pseudopotential basis sets[97]. According to the f-in-core approximation, the electrons of the 4f shells of Eu^{3+}, Tb^{3+}, and Tm^{3+} were incorporated in the pseudopotential. Thus, an explicit treatment of the open 4f shell was not required, which is a major advantage from the computational viewpoint. In the density matrix diagonalization of the bulk calculations, the reciprocal space net was described by a shrinking factor of 4, which corresponds to 36 *k*-points generated according to the Monkhorst–Pack scheme[98]. The accuracy of the evaluation of the Coulomb and exchange series was controlled by five thresholds with values of 10^{-6}, 10^{-6}, 10^{-6}, 10^{-6}, and 10^{-12}.

The initial cell and atomic position parameters used in the optimization process were obtained from the results of the Rietveld refinement of $CaMoO_4$ using a conventional unit cell that contained 24 atoms[10]. The calculation of the equilibrium geometries and electronic properties of the $CaMoO_4$:RE^{3+} (12.5%-doped) system was used to simulate the tetragonal supercell structure of 95 atoms, which corresponds to 2×2×2 conventional cells, in which two Ca^{2+} ions were replaced by two Eu^{3+}, Tb^{3+}, and Tm^{3+} cations, and a calcium vacancy (V_{Ca}) was created to neutralize the unit cell. It should be noted that for the calculation of the doped materials ($CaMoO_4$:RE^{3+}), the experimental percentages of doping were 1mol%, 2mol%, and

4 mol%, as it was necessary to use very large unit cells. The calculations were therefore computationally complex, and a minimum doping amount of 12.5% could be achieved separately for the Eu^{3+}, Tb^{3+}, and Tm^{3+} cations.

The equilibrium shape of the $CaMoO_4$:RE^{3+} microstructures could be determined using the classic Wulff construction[99], which minimizes the total surface free energy at a fixed volume, and provides a simple relationship between the surface energy E_{surf} of the (hkl) plane and its distance in the normal direction from the center of the crystallite. After all the atoms were fully relaxed and the system reached the minimized energy, the surface energies E_{surf} could be calculated using the following expression [92, 100].

$$E_{surf} = (E_{slab} - E_{bulk})/2A \quad (2)$$

Where E_{slab} and E_{bulk} are the total energies of the slab and the bulk with the same number of atoms, respectively, and A represents the surface area of the slab model. The strong dependence of E_{surf} on the surface orientation can be understood with respect to the different distributions of the surface atoms on different surface orientations, given that atomic distribution has a significant influence on the surface electronic structure.

The Wulff construction was successfully used in materials science to obtain the morphologies of materials such as $BaMoO_4$[90], $PbMoO_4$[101], and β-Ag_2MoO_4[102]. To confirm the convergence of the total energy with respect to the slab thicknesses of different surface models, the E_{surf} values for several low-index surfaces were calculated using a 2 × 2 supercell from pure surfaces, and by substituting two Ca^{2+} ions with two Eu^{3+}, Tb^{3+} or Tm^{3+}cations; thus creating a Ca^{2+} vacancy, as expressed in the bulk calculations.

4. RESULTS

The X-ray diffraction patterns of the samples are presented in **Figure 2.** All the diffraction patterns detected were indexed as scheelite-type tetragonal crystal structures with unit cells in space group $I4_1/a$ with C_{4h}^6 symmetries, which is in accordance with the crystallographic card JCPDS 60-5552. This indicates that the rare earth clusters introduced into the matrix did not induce any significant changes in the $CaMoO_4$ structure; however, the density of negative electronic defects was significantly increased. The RE^{3+} ion, when incorporated in the $CaMoO_4$ matrix, results in an excess of positive charges. Hence, the occurrence of Ca^{2+} vacancies is for the neutralization of the charges. As shown in **Figure 2,**

there was a shift in the peak of (112) to the low angle region, due to the increase in the concentration of the RE^{3+} ions. This behavior may be verified by the difference between the electronic density of the Ca^{2+} in relation to the RE^{3+}, which induces distortions and therefore polarization in the clusters [CaO_8]. These changes occur due to the difference in the electronic densities between the forming clusters of the lattice and the doping clusters. The doping process induces the formation of V_{Ca} negatives sites that modify the position of the valence band (VB) energy levels, with concomitant insertion of 4f orbitals of RE^{3+} cations into the conduction band minimum (CBM). As proposed by Almeida et al. [103] and Parchur et al.[42] from the Rietveld refinement conducted on the $CaEu_2(WO_4)_4$ and $CaEu_2(MoO_4)_4$ red phosphors, the $[MoO_4]^{2-}$ tetrahedra in scheelite-structures have high flexibilities. The metal−oxygen distances and bond angles vary significantly with changes in the population of the A-site (in this work A = Ca) by cations with different charges/sizes and/or cation vacancies[104]. However, as shown in **Figure 10**, no major long-term structural changes were observed. Additional peaks identified by at 2θ = 12.87 and 36.65 in the samples doped at 2mol% and 4 mol% of RE^{3+}were observed. These peaks can be attributed to the compound $MoO_n.mH_2O$ formed due to the excessively high solubility of the RE^{3+} in the $CaMoO_4$ matrix, which exceeded the limit[42]. The same tendency was observed in the formation of the secondary phase when 7 mol% and 10 mol% of Eu^{3+} were added to the $CaMoO_4$ structure by the hydrolysis method using urea.

Figure 2.

The Rietveld refinement method was employed to verify possible differences in the structural arrangements obtained using Maud version 2.0 software, and the results of the analysis are presented in **Figure 3**.

Figure 3.

The measured diffraction patterns were in good agreement with the JCPDS 60-5552 standard. An analysis of the diffractograms of the **Figure 3** and the values of the refinement parameters in **Table S1** (Supplementary Information) confirmed the match between the experimental and theoretical data. The results of the refinements are summarized in **Table S1**. In addition, the close correspondence between the lattice parameters and the unit cell volumes reported in literature[98] that $CaMoO_4$ powders have a scheelite-type structure (tetragonal). The introduction of a dopant into a matrix can promote changes in the intensity

and position of the diffraction peaks, as shown in **Figure 2**. These changes occur due to the difference in size between the forming atom of the lattice and the dopant.

Moreover, the scheelite-type tetragonal structure in the primitive cell exhibits 26 different vibration modes: Γ_{Td} = 3Ag + 5Au + 5Bg + 3Bu + 5Eg + 5Eu. However, only Ag, Bg, and Eg are Raman-active, whereas the odd modes 4Au and 4Eu can only be detected in the infrared spectra. The three Bu vibrations are silent modes. In addition, one Au mode and one Eu mode are acoustic vibrations. The micro-Raman spectra of the $CaMoO_4$ and $CaMoO_4:RE^{3+}$ microstructures are presented in **Figure 4**.

Figure 4

The primitive $CaMoO_4$ cell includes two formula units with a weak coupling between the $[MoO_4]^{2-}$ moiety and the Ca^{2+} cations, in addition to the presence of strong covalent Mo–O bonds. The external or lattice phonons correspond to the motion of the Ca^{2+} cations and the rigid molecular unit. The $[MoO_4]^{2-}$ tetrahedral ion in the free space exhibits T_d symmetry. The internal vibrational ions correspond to the vibrations within the $[MoO_4]^{2-}$ group, with an immovable center of mass[105].

The Raman spectra revealed well-defined external and internal peaks for the $CaMoO_4$ and $CaMoO_4:RE^{3+}$microstructures, which indicate that the synthesized powders were highly crystallized. The modes of vibration of the scheelite phase in the tetrahedral structure were observed for each sample. Moreover, several peaks were observed, which were associated with the Raman-active internal modes of tetrahedral MoO_4: ν1 (Ag), ν3 (Bg), ν3 (Eg), ν4 (Eg), ν4 (Bg), ν2 (Bg), ν2 (Ag), R (Ag), R (Eg), and external T (BgEgEg).This is in accordance with the findings reported in[20, 106]. Several differences between the Raman spectra of the $CaMoO_4$ and $CaMoO_4:RE^{3+}$microstructures were observed, and these differences can be associated to the changes of Mo-O bond distances provoked by the addition of RE^{3+} to the structure of the $CaMoO_4$ lattice.

In **Figure 5(a-c)** the unit cell and cluster coordination of the scheelite-type $CaMoO_4:RE^{3+}$ (12.5%- doped) employed in this work have been depicted.

Figure 5.

An analysis of the results revealed that the substitution of Ca^{2+} by Eu^{3+}, Tb^{3+},or Tm^{3+} provokes changes of the atomic coordinates of the oxygen anions with concomitant variations in the RE^{3+}—O distances (see **Figure 5 (a-c)**), which indicates the existence of structural and electronic distortions in the [REO_8], [MoO_4], and [CaO_8] clusters. The corresponding values of atomic coordinates (x, y, z) are listed in **Table S2**. The oxygen anions (O1-O6), highlighted in **Figure. 5(a-c),** allow to find a relationship between the bond distances of the oxygen atoms and the RE^{3+}cations in the $CaMoO_4$ structure. It should be noted that the presence of different RE^{3+}cations produces slight structural distortions in the $CaMoO_4$:RE^{3+} microstructures, which shortens the Eu^{3+}—O and Tm^{3+}—O bond distance, as exemplified by the following distance: O1—Eu1 (2.45Å) to O1—Tm1 (2.37Å).

Figure 6.

The calculated band structure and density of states (DOS) projected for the atoms of $CaMoO_4$:RE^{3+} (12.5%) are displayed in **Figure 6(a-c)** and first Brillouin zone of scheelite are shown in **Figure S1**. The projected DOS for RE^{3+}= Eu^{3+}, Tb^{3+}, and Tm^{3+}, (**Figure 6(a-c) right panel**) reveal that the upper levels of the VB mainly consist of O 2p orbitals; whereas the conduction band (CB) is predominantly formed by Mo^{6+} 4d and RE^{3+} 4f orbitals, with a small amount of Ca^{2+} orbitals. In addition, the doping was found to cause a decrease in the energy levels of the CB with respect to the fundamental band gap of pure $CaMoO_4$ (~4.9 eV)[10]; the calculated value is similar to that obtained by V. Panchal et al. [107] and Ryu et al.[108]. The results reveal that both the valence band maximum (VBM) and conduction band maximum (CBM) are sensitive to the substitution of the RE^{3+}cation electronic states, thus creating intermediate energy levels, that can be associated to the presence of 4f orbitals at the CBM. In particular, intermediate electronic levels were introduced into the E_{gap} region, thus reducing the energy value, as shown in the left panel of **Figure. 6(b-c).** An indirect transition was produced along the k-points Z(111) to Γ (000) from the top of the VB to the bottom of the CB in $CaMoO_4$:Tb^{3+} (E_{gap} = 1.17 eV), and an indirect transition was observed along the k-points X (001) to Γ in $CaMoO_4$:Tm^{3+} (E_{gap}= 3.97 eV); although the intermediate level in the band structure for the doped system was flat. However, in the case of $CaMoO_4$:Eu^{3+} (E_{gap}= 4.69 eV), a direct transition was produced along the k-points Γ to Γ from the top of VB to the bottom of the CB (**see Figure S1**).

The experimental values obtained for the fundamental band gap energies of the $CaMoO_4$ and $CaMoO_4$:RE^{3+} microstructures were estimated from the respective diffuse-

reflectance spectra by plotting the square of the Kubelka–Munk function (i.e., $F(R)^2$) as a function of the energy (in eV)[109-110]. The values were determined by extrapolating the linear part of the curve to $F(R)^2 = 0$, as shown in **Figure 7.** The ratio between the molar absorption coefficient (k) and scattering coefficient (s) was estimated from reflectance data using the Kubelka–Munk relationship, as expressed by Equation 3:

$$F = \frac{K}{S} = \frac{(1-R)^2}{2R} \quad (3)$$

where R is the percentage of reflected light. The incident photon energy ($h\nu$) and optical band gap energy (E_g) are related to the transformed Kubelka–Munk function $[F(R)\ h\nu]^n = A\ (h\nu - E_g)$; where E_g is the fundamental band gap energy, A is a constant dependent on the transition probability, and n is the power index related to the optical absorption process. Moreover, n = 1/2 or n = 2 for an indirect or direct allowed transition[110-111], respectively. The corresponding transition for $CaMoO_4$was considered as direct. The E_g values are presented in **Figure 7**.

Figure 7.

The UV-Vis spectra are presented in **Figure 7,** and the value of the band gap energy was within the range of 3.84–3.93 eV. The substitution of Ca^{2+} by RE^{3+} leads to an excess of positive charges in the semiconductor structure. To neutralize these charges, defects of the Ca^{2+}vacancy type (p) occur, and the presence of these defects is responsible for the intermediate levels in the band gap. These levels favor the electronic transitions between the VB and the CB, due to the band gap reduction.

The PL spectra of the pure $CaMoO_4$ and $CaMoO_4$:RE^{3+} are presented in **Figure. 8(a-b)** and **Figure 8(c),** respectively. It is well known that PL emissions[112] can be associated to the structural and electronic distortion in the tetrahedral [MoO_4] cluster[66] with concomitant appearance of intermediate levels of the band gap[113]. For $CaMoO_4$ microstructures obtained at 600°C, a significant number of structural defects in the crystalline lattice is expected, that it is considered a critical factor for the PL properties. Materials with lower crystallinity indexes exhibit a significant number of intermediate energy levels in the band gap region[114]. Under this condition, electronic transitions occur more easily, thus favoring the PL emissions.

Figure 8

An analysis of the results of **Figure 8 (a)** shows that the PL spectra are composed of broad-band emissions covering the visible electromagnetic spectrum in the range 400−650 nm. This kind of emission profile is typical of multilevel and multiphonon processes, where several paths involving the participation of multiple energy states within the band gap. The emission spectra were deconvoluted in order to further elucidate the emission centers and to qualitatively determine the contribution of each visible light component. **Figure 8 (b)** illustrates the results obtained from the deconvolution of the PL profiles[73, 89, 103]. The profile is well-described by the Voigt area function, and an analysis of the results revealed that the percentages of the areas in the green, blue, orange, and red region are approximately 55%, 20%, 19%, and 6%, respectively.

The presence of the dopant ions (Eu^{3+}, Tb^{3+} and Tm^{3+}) in the $CaMoO_4$ matrix were observed. By mapping the distribution of the elements, it is possible to verify the homogeneous distribution of the rare earth ions (Eu^{3+}, Tb^{3+} and Tm^{3+}) in all particles of $CaMoO_4$. This homogeneity in the material is of great importance for the efficiency of the PL behavior. In addition, the EDS spectrum and the mapping of the distribution of the atoms has been included (see **Figure S3**, Supplementary Information).

The PL phenomenon is reported to be significantly dependent on the presence of defects in the lattice**,** which typically arise during the synthesis or heat treatment of the material. Moreover, the $CaMoO_4:RE^{3+}$material with scheelite-type structure demonstrated a strong 4f–4f transitional absorption and emission due to the polarization of the $[MoO_4]^{2-}$ moiety [42, 115]. As discussed in DOS and band structure, the RE^{3+} doping process at $CaMoO_4$ material promotes a decrease in the band gap values, as well as enhance the charge transfer process from the tetragonal $[MoO_4]^{-2}$ moieties to the $[REO_8]$ clusters, as other authors point out[116].

The PL spectra of the $CaMoO_4:RE^{3+}$ phosphors (**Figure 8 (c) left panel**) exhibited characteristics of each dopant–cation (Eu^{3+}, Tb^{3+} Tm^{3+}) emission. Under the excitation of 350 nm, the $^5D_4 \rightarrow {}^7F_6$ and $^5D_4 \rightarrow {}^7F_5$ transitions occurred at wavelengths of 492 nm and 548 nm, respectively, which are associated with the emission of Tb^{3+} [117-118]. This is related to the charge transfer process from the $[TbO_8]$ to the $[MoO_4]^{2-}$ tetragonal clusters, which corresponds to the 4f → 5d transitions [119].The emission peak at 800 nm is attributed to Tm^{3+}, which is associated with the $^3H_4 \rightarrow {}^3H_6$ transition[115]. With respect to Eu^{3+}, $^5D_0 \rightarrow {}^7F_j$ (j = 1, 2, 3 and 4) transitions occurred at respective wavelengths of 596 nm, 614 nm, 661 nm, and 704

nm[117, 119]. The most intense emission band $^5D_0 \rightarrow {}^7F_2$, of Eu^{3+} is known to have an electric dipole, and this type of transition is highly sensitive to the changes that occur around the Eu^{3+}cation. The intensity of different transitions is dependent on the symmetry of the local environment, according to the Judd−Ofelt theory. The analyses of the emission band can provide detailed information on the crystallographic sites occupied by the Eu^{3+}cation. The presence of significantly more intense $^5D_0 \rightarrow {}^7F_2$ transitions in comparison with the $^5D_0 \rightarrow {}^7F_1$ transition indicated a low local symmetry around the Eu^{3+} in $CaMoO_4$.

As shown in the right panel of **Figure 8 (c)**, the emission intensity of the RE^{3+}cations reached its maximum at a concentration of 1 mol% of $RE^{3+}$and then decreased with an increase in the concentration. This effect is due to the proximity of the RE^{3+}cations within the matrix, which favors the non-radiative transitions. Hence, the low PL signal is enhanced by the quenching effect[120]. The electron interactions that occur between dopant ions can be of different origins. Their classification is in good agreement with the **c**ritical **d**istance (**CD**) that separates two adjacent RE^{3+}cations. The migration of non-radiative energy can occur by two distinct mechanisms: (i) Forster resonance energy transfer (multipole-multipole interaction) and (ii) Dexter mechanism (exchange interaction). The Forster resonance energy transfer typically occurs at distances of up to 100 Å. The Dexter mechanism (also known as exchange or coalitional energy transfer) is a dynamic quenching mechanism. Dexter energy transfer is a short-range phenomenon (**CD** = 10 Å) that decreases with e^{-R}, and it is dependent on the spatial overlap of donor and quencher molecular orbitals[120]. The critical energy transfer distance for $CaMoO_4:RE^{3+}$ was estimated using Equation (4), as suggested by Blasse[121], from the parameters of the structure; namely, the unit cell volume (V), number of units of the molecular formula per unit cell (Z), and quenching concentration (Xc).

$$CD = 2\left[\frac{3V}{4Xc\pi Z}\right]^{1/3} \quad (4)$$

With respect to the $CaMoO_4$:1% RE^{3+}, the following values were considered: Z = 4, V= 312.13 $Å^3$, and Xc = 0.01.The calculated CD was 24.60 Å. In general, the exchange interaction preferably occurs in an energy transfer process when the value of CD is within the range of 5–10 Å. In the case of values higher than 10 Å, there is no indication of exchange interactionsby this mechanism. Consequently, other multipolar electrical interactions are responsible for the quenching effect between two more activating ions (RE^{3+}).

Figure 9 presents the Commission International de l'Eclairage (CIE) chromaticity coordinates for the $CaMoO_4:RE^{3+}$ samples, where as **Table 2** lists the values for the CIE coordinates, correlated temperature color (CCT), and CRI of the samples. The CIE coordinates were obtained from spectral distributions that define three tristimulus values: X, Y, and Z. Based on these values, the chromaticity of a certain color can be set using only two coordinates (x', y').

Figure 9.

Table 2.

Following the distribution of the PL emissions of the $CaMoO_4$ and $CaMoO_4:RE^{3+}$samples, the emitted color of each sample could be characterized. The $CaMoO_4$ sample released emission with a yellowish green color, the sample doped with 1% of RE^{3+} released emission with a greenish yellow color. White emission was observed in the samples doped with 2% and 4% of RE^{3+}, due to the simultaneous blue, green, and red emissions of the different dopants: Tm^{3+}, Tb^{3+}, and Eu^{3+}, respectively. The region coordinates of the balanced white light of the chromaticity diagram were in the range of (x = 0.28–0.35) and (y = 0.30–0.37)[122].This indicates the presence of a new single phase of a white light emitter. The correlative color temperature was also obtained by the empirical relationship of McCamy[123]. The CCT results confirmed the emission regions, as described by the chromaticity coordinates. All the samples reached CRI percentages greater than 90%, which indicates that the samples have a high index of reproduction when used as a light source.

From the surface morphology results based on the FE-SEM measurements, the formation of non-uniform, irregular-sized particles of various dimensions was observed, which could be attributed to the Ostwald ripening of small particles due to the increase in the calcination temperature during the spray pyrolysis process. From the FE-SEM images, the modifications in the morphologies of the $CaMoO_4$ and $CaMoO_4:RE^{3+}$microstructures could be identified (**Figure. 10(a-h)**).

Figure 10.

It is believed that the formation of the particle is associated since the initial solution in which the solvation energy of the H_2O molecule promotes the rapid dissociation of the

reactants so that Ca^{2+} and MoO_4^{-2} ions are rapidly solvated. It is common knowledge that the Ca^{2+}cationscoordinate to eight oxygen anions, which forma dodecahedral symmetry [CaO_8]. The Mo^{6+}cations are coordinated with four oxygen anions to form a tetrahedral configuration [MoO_4]. Due to the difference between the electronic densities of the [CaO_8] and [MoO_4] clusters, there is a strong electrostatic attraction between them. **Figure 1** presents a schematic of all the steps involved in the growth of the $CaMoO_4$ and $CaMoO_4$:RE^{3+} microstructures obtained using the spray pyrolysis method.

For all the samples in this study, to which RE^{3+} was added (**Figure. 10 (c-h)**), the particles had distorted shapes and exhibited irregular morphologies. Moreover, they were formed by a cluster of polycrystalline particles in which some were dense, and broken particles with holes were observed. All these irregularities in the morphologies were due to the addition of rare earths to the $CaMoO_4$ matrix that modify particle surfaces. In addition, the final formation process of the particles using the spray pyrolysis method may promote the emergence of these defects. This was not the case for the particles of pure $CaMoO_4$ at 600°C (**Figure 10 (a-b)**), which had defect-free surfaces with several cracks due to the rapid formation involved in the pyrolysis spray process.

According to previous calculations, the surface energy of the (001), (112), (110), (101), (100), and (111) surfaces are 0.72J/m^2, 0.75J/m^2,0.93J/m^2, 1.01J/m^2, 1.15J/m^2, and 4.56 J/m^2, respectively. Therefore, the order of stability in the pure $CaMoO_4$ is as follows: (001)<(112)<(110)<(101)<(100)[10]. The geometry of the (001), (100), (110), (101), and (112) surfaces of the $CaMoO_4$:12.5% Eu^{3+} system are presented in **Figure S2** (Supplementary Information).Given that the stability of the (111) surface was reduced when compared with the remaining planes in pure $CaMoO_4$ due to under-coordination at the [MoO_2] cluster[115], this plane was not evaluated in this study. Moreover, the order of stability of the surfaces was found to be (100)<(001)<(112)<(110)<(101). This order was maintained for the three systems at 12.5% with minimal differences between the E_{surf} values (see **Table S3** in the Supplementary Information). The ideal morphologies of the $CaMoO_4$:12.5%RE^{3+} microstructures are presented in **Figure 11(a)** using Wulff construction, which differs from those of pure $CaMoO_4$ due to the large stabilization of the (100) surface. The available morphologies of the $CaMoO_4$:Eu^{3+} system can be obtained by modifying the relative E_{surf} values for each surface, as shown in **Figure 11(b)**. In this map, from the ideal morphology and by an increase in the E_{surf} value of the (100) surface, a similar morphology, (1) to that of pure $CaMoO_4$ was achieved; and by an increase in the E_{surf} value of the (112) surface, a cubic morphology (2); by a decrease in the E_{surf} values for the (112) surface, their presence in the

morphology increases, i.e. (3); and by a decrease in the E_{surf} values of the (110) surface, the morphology (4) could be obtained.

In our previous work[10], as well as in other theoretical and experimental studies[95-96,124-125] the same methodology was proposed to investigate the morphological modulations of different compounds. Therefore, based on this procedure, we can rationalize the morphological transformation imposed by the RE^{3+} doping process. **Figure 11** displays the main changes caused by rare earth doping in surface energy values, enabling to predict a plethora of available morphologies for doped $CaMoO_4$.

Finally, it is important to remark that in recent years, a near ultraviolet (n-UV) LEDs chip (350-420 nm) has been extensively investigated, which combined with blue, green and red emitting phosphors, to obtain an increased color reproduction index with controllable emitter colors[126-128]. This work presents $CaMoO_4:RE^{3+}$ samples as promising candidates to this end.

5. CONCLUSIONS

In summary, $CaMoO_4$ and $CaMoO_4:xRE^{3+}$((RE^{3+} = Eu^{3+}, Tb^{3+}, and Tm^{3+}; and x= 1%, 2%, and 4%l) compounds with tunable PL emissions and morphologies were successfully synthetized using the spray pyrolysis method. The XRD results revealed that no deleterious phases were present, which confirmed the purity of the samples, and the dopants were then introduced into the matrix. The Raman scattering spectra for the $CaMoO_4$and $CaMoO_4:RE^{3+}$ powders exhibited well-defined peaks for the external and internal modes, and the vibration modes of the scheelite phase was observed in the tetrahedral structures of all the samples.

The analysis of the results obtained from first principle calculation, at density functional theory level, allows us to rationalize the electronic and optical properties of the as-synthetized samples. In addition, the calculations of the surface energies, based on Wulff construction, explain the morphology transformation of the $CaMoO_4$ and $CaMoO_4:RE^{3+}$ microstructures, observed in the FE-SEM images. PL measurements point out that the presence of the particular signatures of the RE^{3+} cations, i.e. 615 nm for the $^5D_0 \rightarrow {}^7F_2$ transition of Eu^{3+}, 545 nm for the $^5D_4 \rightarrow {}^7F_5$ transition of Tb^{3+}, and 800 nm for the $^3H_4 \rightarrow {}^3H_6$ transition of Tm^{3+}, as well as reveal new white light emitter due to the formation of $CaMoO_4:RE^{3+}$ composites. In particular, the chromaticity coordinates of $CaMoO_4:RE^{3+}$ indicated that the samples doped with 2% and 4% of RE^{3+} display white emissions, which are promising candidates for visual displays and solid-state lighting**.** Hence, these materials can

demonstrate better performances with certain modifications; thus providing a platform to tune the optical properties.

NOTES

Supplementary Information contains: Rietveld refined structural parameters; theoretical atomics coordinates; surface energy values; path Brillouin Zone and amplified band structure and total DOS projected; surfaces models, chemical analysis of x-ray spectroscopy by dispersive energy and mapping of the distribution of atoms.

ACKNOWLEDGMENTS

The authors thank the following Brazilian and Spanish research financing institutions for financial support: National Council for Scientific and Technological Development - CNPq (Processo 402127/2013-7), Sao Paulo Research Foundation - FAPESP (Processo 2013/07296-2),(2016/23891-6), Programa de Pós-Graduação em Ciência e Engenharia de Materiais (PPGCEM-UFRN) and Coordenação de Aperfeiçoamento de Pessoal de Nível Superior - Brasil (CAPES) - Finance Code 001, Universitat Jaume I for project UJIB2016-25, GeneralitatValenciana (PrometeoII/2014/022, ACOMP/2014/270, and ACOMP/2015/1202), Ministerio de Economía y Competitividad, Spain (project CTQ2015-65207-P). M.C.Oliveira acknowledges Generalitat Valenciana for Santiago Grisolia Program 2015/033 and CAPES (2019/88887.319041) for the financial support. We also acknowledge the Servei Informática, Universitat Jaume I for a generous allotment of computer time. The authors thank to Enio Longo for the support with the scientific illustrations.

REFERENCES

1. Laubsch, A.; Sabathil, M.; Baur, J.; Peter, M.; Hahn, B., High-Power and High-Efficiency Ingan-Based Light Emitters. *IEEE Trans. Electron Devices* **2010**, *57*, 79-87.
2. Lovisa, L. X.; Araújo, V. D.; Tranquilin, R. L.; Longo, E.; Li, M. S.; Paskocimas, C. A.; Bomio, M. R. D.; Motta, F. V., White Photoluminescence Emission from ZrO_2 Co-Doped with Eu^{3+}, Tb^{3+} and Tm^{3+}. *J. Alloy.Compd.* **2016**, *674*, 245-251.
3. Huang, C.-H.; Liu, W.-R.; Chen, T.-M., Single-Phased White-Light Phosphors $Ca_9Gd(PO_4)_7$:Eu^{2+},Mn^{2+} under near-Ultraviolet Excitation. *J. Phys. Chem. C* **2010**, *114*, 18698-18701.
4. Park, S.; Koh, S.; Kim, H., Single-Phase Ce^{3+}–Mn^{2+}–Tb^{3+} Tri–Codoped Barium–Yttrium–Silicate Phosphors. *Displays*. **2017**, *48*, 29-34.
5. Luévano-Hipólito, E.; Torres-Martínez, L. M., Ink-Jet Printing Films of Molybdates of Alkaline Earth Metals with Scheelite Structure Applied in the Photocatalytic CO_2 Reduction. *J. Photoch. Photobio. A* **2019**, *368*, 15-22.
6. Zhu, Y.; Zheng, G.; Dai, Z.; Zhang, L.; Ma, Y., Photocatalytic and Luminescent Properties of $SrMoO_4$ Phosphors Prepared Via Hydrothermal Method with Different Stirring Speeds. *J. Mater. Sci.Technol.* **2017**, *33*, 23-29.
7. Hosseinpour-Mashkani, S. S.; Hosseinpour-Mashkani, S. S.; Sobhani-Nasab, A., Synthesis and Characterization of Rod-Like $CaMoO_4$ Nanostructure Via Free Surfactant

Sonochemical Route and Its Photocatalytic Application. *J. Mater. Sci.: Mater. Electron.* **2016**, *27*, 4351-4355.
8. Gholami, A.; Maddahfar, M., Synthesis and Characterization of Barium Molybdate Nanostructures with the Aid of Amino Acids and Investigation of Its Photocatalytic Degradation of Methyl Orange. *J. Mater. Sci.: Mater. Electron.* **2016**, *27*, 6773-6778.
9. De Santana, Y. V. B.; Gomes, J. E. C.; Matos, L.; Cruvinel, G. H.; Perrin, A.; Perrin, C.; Andrès, J.; Varela, J. A.; Longo, E., Silver Molybdate and Silver Tungstate Nanocomposites with Enhanced Photoluminescence. *Nanomater. Nanotechn.* **2014**, *4*, 22.
10. Oliveira, F. K. F.; Oliveira, M. C.; Gracia, L.; Tranquilin, R. L.; Paskocimas, C. A.; Motta, F. V.; Longo, E.; Andrés, J.; Bomio, M. R. D., Experimental and Theoretical Study to Explain the Morphology of $CaMoO_4$ Crystals. *J. Physi. Chem. Solids* **2018**, *114*, 141-152.
11. Musikhin, A. E.; Naumov, V. N.; Chislov, M. V.; Zvereva, I. A., Thermodynamic Properties of $CaMoO_4$ at High Temperatures. *Thermochim. Acta* **2018**, *661*, 160-165.
12. Dutta, S.; Som, S.; Sharma, S. K., Optimization and Characterization of Trap Level Distribution in Γ-Irradiated Doped/Codoped $CaMoO_4$ Phosphors. *Phys. B: Condensed Matter* **2013**, *417*, 39-45.
13. Wu, H.; Hu, Y.; Zhang, W.; Kang, F.; Li, N.; Ju, G., Sol–Gel Synthesis of Eu^{3+} Incorporated $CaMoO_4$: The Enhanced Luminescence Performance. *J. Sol-Gel Sci. Technol.* **2012**, *62*, 227-233.
14. Xie, A.; Yuan, X.; Hai, S.; Wang, J.; Wang, F.; Li, L., Enhancement Emission Intensity of $CaMoO4:Eu^{3+}$, Na^{+} Phosphor Via Bi Co-Doping and Si Substitution for Application to White Leds. *J. Phys. D: Appl. Phys.* **2009**, *42*, 105107.
15. Zhang, Z. H.; Huang, Q.; Zhao, X.; Huang, Z. L., Enhanced Red Emission of $CaMoO_4$:Eu^{3+} Phosphor by Structural Adjustment for White Light-Emitting Diodes Application. *Phys. Stat. Sol* **2009**, *206*, 2839-2843.
16. Vukasovich, M. S.; Farr, J. P. G., Molybdate in Corrosion Inhibition a Review. *Polyhedron* **1986**, *5*, 551-559.
17. Xie, Y.; Ma, S.; Wang, Y.; Xu, M.; Lu, C.; Xiao, L.; Deng, S., Controlled Synthesis and Luminescence Properties of $CaMoO_4$:Eu^{3+} Microcrystals. *Opt. Mater.* **2018**, *77*, 13-18.
18. Ming, X.; Meng, Q.; Xiong, J.; Sun, W., Study on the Color Tunability and Energy Transfer Mechanism in Tb^{3+}, Sm^{3+} Co-Doped $CaMoO_4$ Phosphors. *J. Alloy. Compds.* **2017**, *695*, 1691-1698.
19. Wang, L.; Song, Q.; Guo, X.; Wang, N.; Wang, X.; Han, Y.; Xie, J., Synthesis of Hollow Spindle-Like $CaMoO_4$: Ln^{3+}(Tb, Eu) Phosphors for Detection of Iron(Ⅲ) Ions. *Optik* **2019**, *185*, 957-964.
20. Phuruangrat, A.; Thongtem, T.; Thongtem, S., Preparation, Characterization and Photoluminescence of Nanocrystalline Calcium Molybdate. *J. Alloy. Compd.* **2009**, *481*, 568-572.
21. Laguna, M.; Nuñez, N. O.; Becerro, A. I.; Ocaña, M., Morphology Control of Uniform $Camoo_4$ Microarchitectures and Development of White Light Emitting Phosphors by Ln Doping (Ln = Dy^{3+}, Eu^{3+}). *CrystEngComm* **2017**, *19*, 1590-1600.
22. Saraf, R.; Shivakumara, C.; Dhananjaya, N.; Behera, S.; Nagabhushana, H., Photoluminescence Properties of Eu^{3+}-Activated $CaMoO_4$ Phosphors for Wleds Applications and Its Judd–Ofelt Analysis. *J. Mater. Sci.* **2015**, *50*, 287-298.
23. Zhang, Z.-J.; Chen, H.-H.; Yang, X.-X.; Zhao, J.-T., Preparation and Luminescent Properties of Eu^{3+} and Tb^{3+} Ions in the Host of $CaMoO_4$. *Mater. Sci. Eng. B* **2007**, *145*, 34-40.
24. Kozlova, N. S.; Buzanov, O. A.; Kozlova, A. P.; Zabelina, E. V.; Goreeva, Z. A.; Didenko, I. S.; Kasimova, V. M.; Chernykh, A. G., Optical Properties and Microdefects in $CaMoO_4$ Single Crystals. *Crystallogr. Rep.* **2018**, *63*, 216-221.

25. Huerta-Flores, A. M.; Juárez-Ramírez, I.; Torres-Martínez, L. M.; Carrera-Crespo, J. E.; Gómez-Bustamante, T.; Sarabia-Ramos, O., Synthesis of $AMoO_4$ (A = Ca, Sr, Ba) Photocatalysts and Their Potential Application for Hydrogen Evolution and the Degradation of Tetracycline in Water. *J. Photoch. Photobio. A* **2018**, *356*, 29-37.
26. Marques, V. S.; Cavalcante, L. S.; Sczancoski, J. C.; Alcântara, A. F. P.; Orlandi, M. O.; Moraes, E.; Longo, E.; Varela, J. A.; Siu Li, M.; Santos, M. R. M. C., Effect of Different Solvent Ratios (Water/Ethylene Glycol) on the Growth Process of $CaMoO_4$ Crystals and Their Optical Properties. *Cryst. Growth Des.* **2010**, *10*, 4752-4768.
27. Sun, Y.; Li, C.; Zhang, Z.; Ma, X.; Wang, L.; Wang, Y.; Song, M.; Ma, P.; Jiang, L.; Guo, Y., Persimmon-Like $CaMoO_4$ Micro/Nanomaterials: A Rapid Microwave-Assisted Fabrication, Characterization, and the Growth Mechanism. *Solid State Sci.* **2012**, *14*, 219-224.
28. Choi, H.; Kim, D.; Yoon, S. P.; Han, J.; Ha, S.; Kim, J., Production of Molybdenum Oxide Particles with High Yield by Ultrasonic Spray Pyrolysis and Their Catalytic Activity toward Partial Oxidation of N-Dodecane. *J. Anal. Appl. Pyrol.* **2015**, *112*, 276-283.
29. Huang, Y.; Gao, Y.; Zhang, Q.; Cao, J.-j.; Huang, R.-j.; Ho, W.; Lee, S. C., Hierarchical Porous $ZnWO_4$ Microspheres Synthesized by Ultrasonic Spray Pyrolysis: Characterization, Mechanistic and Photocatalytic Nox Removal Studies. *Appl. Catal. A: Gen.* **2016**, *515*, 170-178.
30. Mikhailik, V. B.; Henry, S.; Kraus, H.; Solskii, I., Temperature Dependence of $Camoo_4$ Scintillation Properties. *Nucl.Instrum.Meth. Phys. Res. A.* **2007**, *583*, 350-355.
31. Mikhailik, V. B.; Kraus, H.; Miller, G.; Mykhaylyk, M. S.; Wahl, D., Luminescence of $Cawo_4$, $Camoo_4$, and $ZnWO_4$ Scintillating Crystals under Different Excitations. *J. Appl. Phys.* **2005**, *97*, 083523.
32. Raju, G. S. R.; Pavitra, E.; Ko, Y. H.; Yu, J. S., A Facile and Efficient Strategy for the Preparation of Stable $CaMoO_4$ Spherulites Using Ammonium Molybdate as a Molybdenum Source and Their Excitation Induced Tunable Luminescent Properties for Optical Applications. *J. Mater. Chem.* **2012**, *22*, 15562-15569.
33. Xiao, B.; Schmidt, M., Incorporation of Europium(III) into Scheelite-Related Host Matrixes ABO_4 (A = Ca^{2+}, Sr^{2+}, Ba^{2+}; B = W^{6+}, Mo^{6+}): Role of a and B Sites on the Dopant Site Distribution and Photoluminescence. *Inorg. Chem.* **2017**, *56*, 14948-14959.
34. Dey, R.; Kumar Rai, V., Er^{3+}-Tm^{3+}-Yb^{3+}:$CaMoO_4$ phosphor as an Outstanding Upconversion-Based Optical Temperature Sensor and Optical Heater. *Methods Appl. Fluores.* **2017**, *5*, 015006.
35. Verma, A.; Sharma, S. K., Down-Conversion from Er^{3+}-Yb^{3+} Codoped $CaMoO_4$ Phosphor: A Spectral Conversion to Improve Solar Cell Efficiency. *Ceram. Inter.* **2017**, *43*, 8879-8885.
36. Zheng, Y.; Huo, J.; Yang, J.; Hu, J.; Gao, J.; Wang, Q., Extensive Studies of Host Lattices and Activators in Lanthanide Phosphors Based on Efficient Synthesis. *J. Alloy. Compd.* **2016**, *676*, 292-298.
37. Campos, A. B.; Simões, A. Z.; Longo, E.; Varela, J. A.; Longo, V. M.; Figueiredo, A. T. d.; Vicente, F. S. D.; Hernandes, A. C., Mechanisms Behind Blue, Green, and Red Photoluminescence Emissions in $CaWO_4$ and $CaMoO_4$ Powders. *Appl. Phys. Lett.* **2007**, *91*, 051923.
38. Li, L.; Su, Y.; Li, G., Size-Induced Symmetric Enhancement and Its Relevance to Photoluminescence of Scheelite $CaWO_4$ Nanocrystals. *Appl. Phys. Lett.* **2007**, *90*, 054105.
39. Kato, A.; Oishi, S.; Shishido, T.; Yamazaki, M.; Iida, S., Evaluation of Stoichiometric Rare-Earth Molybdate and Tungstate Compounds as Laser Materials. *J. Phys. Chem. Solid.* **2005**, *66*, 2079-2081.

40. Kuisheng, Y.; Yan, L.; Chaoyi, Y.; Liping, L.; Chanhua, Y.; Xiyan, Z., Upconversion Luminescence Properties of Ho^{3+}, Tm^{3+}, Yb^{3+} Co-Doped Nanocrystal NaYF4 Synthesized by Hydrothermal Method. *J. Rare Earths* **2006**, *24*, 757-760.
41. Dai, P., Enhanced Red Emission Induced by Tb^{3+} Doping in Europium-Based Molybdate Phosphors. *Mater. Res. Bull.* **2017**, *94*, 64-69.
42. Parchur, A. K.; Ningthoujam, R. S., Preparation and Structure Refinement of Eu^{3+} Doped $CaMoO_4$ Nanoparticles. *Dalton Trans.* **2011**, *40*, 7590-7594.
43. Mendoza, C.; Ligny, D. d.; Panczer, G.; Peuget, S.; Bardez-Giboire, I.; Schuller, S., Behaviour of the Eu^{3+} $^5d_0 \rightarrow {}^7f_0$ Transition in $CaMoO_4$ Powellite Type Ceramics under Ar and Pb Ions Implantation. *Opt. Mater.* **2011**, *34*, 386-390.
44. Ho Ryu, J.; Geun Choi, B.; Yoon, J.-W.; Bo Shim, K.; Machi, K.; Hamada, K., Synthesis of $CaMoO_4$ Nanoparticles by Pulsed Laser Ablation in Deionized Water and Optical Properties. *J. Lumin.* **2007**, *124*, 67-70.
45. Hou, Z.; Chai, R.; Zhang, M.; Zhang, C.; Chong, P.; Xu, Z.; Li, G.; Lin, J., Fabrication and Luminescence Properties of One-Dimensional $CaMoO_4$: Ln^{3+} (Ln = Eu, Tb, Dy) Nanofibers Via Electrospinning Process. *Langmuir* **2009**, *25*, 12340-12348.
46. Ningthoujam, R. S., *Enhancement of Luminescence by Rare Earth Ions Doping in Semiconductor Host.* ; Ed. S. B. Rai and Y. Dwivedi; Nova Science Publishers, Inc.: Hauppauge: USA, 2012.
47. Han, L.; Pan, M.; Lv, Y.; Gu, Y.; Wang, X.; Li, D.; Kong, Q.; Dong, X., Fabrication of Y_2O_2S:Eu^{3+} Hollow Nanofibers by Sulfurization of Y_2O_3:Eu^{3+} Hollow Nanofibers. *J. Mater. Sci.: Mater. Electron.* **2015**, *26*, 677-684.
48. Kitai, A. H., *Luminescent Materials and Applications*; Ed. John Wiley & Sons: Canada, 2008.
49. Ren, W.; Wen, S.; Tawfik, S. A.; Su, Q. P.; Lin, G.; Ju, L. A.; Ford, M. J.; Ghodke, H.; van Oijen, Antoine M.; Jin, D., Anisotropic Functionalization of Upconversion Nanoparticles. *Chem. Sci.* **2018**, *9*, 4352-4358.
50. Zhang, Y.; Geng, D.; Shang, M.; Zhang, X.; Li, X.; Cheng, Z.; Lian, H.; Lin, J., Soft-Chemical Synthesis and Tunable Luminescence of Tb^{3+}, Tm^{3+}/Dy^{3+}-Doped SrY_2O_4 Phosphors for Field Emission Displays. *Dalton Trans.* **2013**, *42*, 4799-4808.
51. Kang, F.; Zhang, Y.; Peng, M., Controlling the Energy Transfer Via Multi Luminescent Centers to Achieve White Light/Tunable Emissions in a Single-Phased X2-Type Y_2SiO_5:Eu^{3+},Bi^{3+} Phosphor for Ultraviolet Converted Leds. *Inorg. Chem.* **2015**, *54*, 1462-1473.
52. Yadav, R. S.; Rai, S. B., Structural Analysis and Enhanced Photoluminescence Via Host Sensitization from a Lanthanide Doped $BiVO_4$ Nano-Phosphor. *J. Phys. Chem. Solid.* **2017**, *110*, 211-217.
53. Wang, F.; Han, Y.; Lim, C. S.; Lu, Y.; Wang, J.; Xu, J.; Chen, H.; Zhang, C.; Hong, M.; Liu, X., Simultaneous Phase and Size Control of Upconversion Nanocrystals through Lanthanide Doping. *Nature* **2010**, *463*, 1061.
54. Pinatti, I. M.; Pereira, P. F. S.; de Assis, M.; Longo, E.; Rosa, I. L. V., Rare Earth Doped Silver Tungstate for Photoluminescent Applications. *J. Alloy. Compd.* **2019**, *771*, 433-447.
55. Piskuła, Z.; Staninski, K.; Lis, S., Luminescence Properties of Tm^{3+}/Yb^{3+}, Er^{3+}/Yb^{3+} and Ho^{3+}/Yb^{3+} Activated Calcium Tungstate. *J. Rare Earths* **2011**, *29*, 1166-1169.
56. Piskuła, Z.; Czajka, J.; Staninski, K.; Lis, S., Luminescence Properties of Calcium Tungstate Activated by Lanthanide(III) Ions. *J. Rare Earths* **2014**, *32*, 221-225.
57. Li, S.; Meng, Q.; Lü, S.; Sun, W., Study on Optical Temperature Sensing Properties of Tb^{3+}, Eu^{3+} Co-Doped $CaMoO_4$ Phosphor. *J. Lumin.* **2018**, *200*, 103-110.

58. Ningthoujam, R. S., Generation of Exciton in Two Semiconductors Interface: SnO_2:Eu–Y_2O_3. *Chem. Phys. Lett.* **2010**, *497*, 208-212.
59. Sharma, K. G.; Singh, T. P.; Singh, N. R., Low Temperature Synthesis, Characterization and Tunable Optical Properties of Eu^{3+}, Tb^{3+} Doped $CaMoO_4$ Nanoparticles. *J. Alloy. Compd.* **2014**, *602*, 275-280.
60. Bharat, L. K.; Raju, G. S. R.; Yu, J. S., Red and Green Colors Emitting Spherical-Shaped Calcium Molybdate Nanophosphors for Enhanced Latent Fingerprint Detection. *Scientific Reports* **2017**, *7*, 11571.
61. Khanna, A.; Dutta, P. S., Narrow Spectral Emission Camoo$_4$: Eu^{3+}, Dy^{3+}, Tb^{3+} Phosphor Crystals for White Light Emitting Diodes. *J. Solid State Chem.* **2013**, *198*, 93-100.
62. Gupta, S. K.; Sahu, M.; Ghosh, P. S.; Tyagi, D.; Saxena, M. K.; Kadam, R. M., Energy Transfer Dynamics and Luminescence Properties of Eu^{3+} in $CaMoO_4$ and $SrMoO_4$. *Dalton Trans.* **2015**, *44*, 18957-18969.
63. Liu, X.; Li, L.; Noh, H. M.; Jeong, J. H.; Jang, K.; Shin, D. S., Controllable Synthesis of Uniform $CaMoO_4$:Eu^{3+},M^+ (M = Li, Na, K) Microspheres and Optimum Luminescence Properties. *RSC Adv.* **2015**, *5*, 9441-9454.
64. Hazra, C.; Samanta, T.; Asaithambi, A. V.; Mahalingam, V., Bilayer Stabilized Ln^{3+}-Doped $CaMoO_4$ Nanocrystals with High Luminescence Quantum Efficiency and Photocatalytic Properties. *Dalton Trans.* **2014**, *43*, 6623-6630.
65. Singh, B. P.; Parchur, A. K.; Ningthoujam, R. S.; Ansari, A. A.; Singh, P.; Rai, S. B., Influence of Gd^{3+} Co-Doping on Structural Property of $CaMoO_4$:Eu Nanoparticles. *Dalton Trans.* **2014**, *43*, 4770-4778.
66. Xiong, J.; Meng, Q.; Sun, W., Luminescent Properties and Energy Transfer Mechanism from Tb^{3+} to Eu^{3+} in $CaMoO_4$:Tb^{3+},Eu^{3+} Phosphors. *J. Rare Earths* **2016**, *34*, 251-258.
67. Chung, J. H.; Ryu, J. H.; Mhin, S. W.; Kim, K. M.; Shim, K. B., Controllable White Upconversion Luminescence in Ho^{3+}/Tm^{3+}/Yb^{3+} Co-Doped $CaMoO_4$. *J. Mater. Chem.* **2012**, *22*, 3997-4002.
68. Han, Y.; Wang, L.; Wang, D.; Liang, D.; Wang, S.; Lu, G.; Di, Z.; Jia, G., Lanthanide Ions-Doped Calcium Molybdate Pie-Like Microstructures: Synthesis, Structure Characterization, and Luminescent Properties. *J. Alloy. Compd.* **2017**, *695*, 3018-3023.
69. Wang, X.-F.; Peng, G.-H.; Li, N.; Liang, Z.-H.; Wang, X.; Wu, J.-L., Hydrothermal Synthesis and Luminescence Properties of 3d Walnut-Like $CaMoO_4$:Eu^{3+} Red Phosphors. *J. Alloy. Compd.* **2014**, *599*, 102-107.
70. Li, J.; Zhang, T.; Zhu, G.; Hairong, Z., Up-Conversion Photoluminescence Emissions of $CaMoO_4$:Pr^{3+}/Yb^{3+} Powder. *J. Rare Earths* **2017**, *35*, 645-651.
71. Li, S.; Yu, L.; Sun, J.; Man, X., Synthesis and Photoluminescent Characteristics of Eu^{3+}-Doped $MMoO_4$ (M=Sr, Ba) Nanophosphors by a Hydrothermal Method. *J. Rare Earths* **2017**, *35*, 347-3355.
72. Ansari, A. A.; Alam, M., Optical and Structural Studies of $CaMoO_4$:Sm, $CaMoO_4$:Sm@$CaMoO_4$ and $CaMoO_4$:Sm@$CaMoO_4$@SiO_2 Core–Shell Nanoparticles. *J. Lumin.* **2015**, *157*, 257-263.
73. Gurgel, G. M.; Lovisa, L. X.; Pereira, L. M.; Motta, F. V.; Li, M. S.; Longo, E.; Paskocimas, C. A.; Bomio, M. R. D., Photoluminescence Properties of (Eu, Tb, Tm) Co-Doped $PbMoO_4$ Obtained by Sonochemical Synthesis. *J. Alloy. Compd.* **2017**, *700*, 130-137.
74. Chung, W.; Jeong Yu, H.; Hee Park, S.; Chun, B.-H.; Kim, J.; Hyun Kim, S., Spray Pyrolysis Synthesis of MAl_2O_4:Eu^{2+} (M=Ba, Sr) Phosphor for UV Led Excitation. *J. Cryst. Growth* **2011**, *326*, 73-76.

75. Zhai, Y.; Zhao, X.; Liu, C.; Song, P.; Jing, X.; Han, Y.; Wang, J., $CaMoO_4:Dy^{3+},Eu^{3+}$ Phosphors: Microwave Synthesis, Characterization, Tunable Luminescence Properties and Energy Transfer Mechanism. *Optik* **2018**, *164*, 433-442.
76. Lou, Z.; Cocivera, M., Cathodoluminescence of $CaWO_4$ and $SrWO_4$ Thin Films Prepared by Spray Pyrolysis. *Mater.als Res. Bull.* **2002**, *37*, 1573-1582.
77. Biskos, G.; Vons, V.; Yurteri, C. U.; Schmidt-Ott, A., Generation and Sizing of Particles for Aerosol-Based Nanotechnology. *KONA Powder Part. J.* **2008**, *26*, 13-35.
78. De Melo, M. M.; Motta, F. V.; Bomio, M. R. D.; Almeida, M. C. D.; De Melo, A. S. P.; Paskocimas, C. A., The Addition of Urea in the Ultrasonic Spray Pyrolysis Process and Its Influence on the Morphology of the Products Obtained. . *Int. J. Sci. Adv. Technol.* **2014**, *4*, 1-5.
79. Kang, Y. C.; Park, S. B., Preparation of Nanometre Size Oxide Particles Using Filter Expansion Aerosol Generator. *J. Mater. Sci.* **1996**, *31*, 2409-2416.
80. Li, Y.; Li, X.; Wang, Z.; Guo, H.; Li, T., Distinct Impact of Cobalt Salt Type on the Morphology, Microstructure, and Electrochemical Properties of Co_3O_4 Synthesized by Ultrasonic Spray Pyrolysis. *J. Alloy. Compd.* **2017**, *696*, 836-843.
81. Choi, H.; Yoon, S. P.; Han, J.; Kim, J.; Othman, M. R., Continuous Synthesis of Molybdenum Oxide Microspheres by Ultrasonic Spray Pyrolysis. *J. Ind. Eng. Chem.* **2017**, *47*, 254-259.
82. Afify, H. H.; Hassan, S. A.; Abouelsayed, A.; Demian, S. E.; Zayed, H. A., Coloration of Molybdenum Oxide Thin Films Synthesized by Spray Pyrolysis Technique. *Thin Solid Films* **2017**, *623*, 40-47.
83. Brunetti, F., *Mechanics of Fluids*; Ed. Pearson Prentice: São Paulo, 2008.
84. Zhou, Y.; Liu, J.; Yang, X.; Yu, X.; Wang, L., Self-Assembly and Photoluminescence Characterization of $CaMoO_4: Eu^{3+}, Na^{+}$ Superstructure Via a Facile Surfactant-Free Hydrothermal Method. *J. Elect. Soc.* **2011**, *158*, K74-K80.
85. Lee, C.; Yang, W.; Parr, R. G., Development of the Colle-Salvetti Correlation-Energy Formula into a Functional of the Electron Density. *Phys. Rev. B: Condens. Matter* **1988**, *37*, 785-789.
86. Becke, A. D., Density-Functional Thermochemistry. Iii. The Role of Exact Exchange. *J. Chem. Phys.* **1993**, *98*, 5648-5652.
87. Dovesi, R., et al., Quantum-Mechanical Condensed Matter Simulations with Crystal. *Comput.Mol.Sci.* **2018**, *8*, e1360.
88. Fabbro, M. T.; Saliby, C.; Rios, L. R.; La Porta, F. A.; Gracia, L.; Li, M. S.; Andrés, J.; Santos, L. P. S.; Longo, E., Identifying and Rationalizing the Morphological, Structural, and Optical Properties of B-Ag_2MoO_4 Microcrystals, and the Formation Process of Ag Nanoparticles on Their Surfaces: Combining Experimental Data and First-Principles Calculations. *Sci. Technol. Adv. Mater.* **2015**, *16*, 065002.
89. Lovisa, L. X.; Oliveira, M. C.; Andrés, J.; Gracia, L.; Li, M. S.; Longo, E.; Tranquilin, R. L.; Paskocimas, C. A.; Bomio, M. R. D.; Motta, F. V., Structure, Morphology and Photoluminescence Emissions of $ZnMoO_4$: RE $^{3+}$=Tb^{3+} - Tm^{3+} - X Eu^{3+} (X = 1, 1.5, 2, 2.5 and 3 Mol%) Particles Obtained by the Sonochemical Method. *J. Alloy. Compd.* **2018**, *750*, 55-70.
90. Oliveira, M. C.; Gracia, L.; Nogueira, I. C.; Gurgel, M. F. C.; Mercury, J. M. R.; Longo, E.; Andrés, J., On the Morphology of $BaMoO_4$ Crystals: A Theoretical and Experimental Approach. *Cryst. Res. Technol.* **2016**, *51*, 634-644.
91. Gracia, L.; Longo, V. M.; Cavalcante, L. S.; Beltrán, A.; Avansi, W.; Li, M. S.; Mastelaro, V. R.; Varela, J. A.; Longo, E.; Andrés, J., Presence of Excited Electronic State in $CaWO_4$ Crystals Provoked by a Tetrahedral Distortion: An Experimental and Theoretical Investigation. *J. Appl. Phys.* **2011**, *110*, 043501.

92. Oliveira, M. C.; Andrés, J.; Gracia, L.; de Oliveira, M. S. M. P.; Mercury, J. M. R.; Longo, E.; Nogueira, I. C., Geometry, Electronic Structure, Morphology, and Photoluminescence Emissions of $BaW_{1-X}Mo_xO4$ (X = 0, 0.25, 0.50, 0.75, and 1) Solid Solutions: Theory and Experiment in Concert. *Appl. Surf. Sci.* **2019**, *463*, 907-917.
93. Gouveia, A. F.; Ferrer, M. M.; Sambrano, J. R.; Andrés, J.; Longo, E., Modeling the Atomic-Scale Structure, Stability, and Morphological Transformations in the Tetragonal Phase of $LaVO_4$. *Chem. Phys. Lett.* **2016**, *660*, 87-92.
94. Beltrán, A.; Gracia, L.; Andrés, J.; Longo, E., First-Principles Study on Polymorphs of $AgVO_3$: Assessing to Structural Stabilities and Pressure-Induced Transitions. *J. Phys. Chem. C.* **2017**, *121*, 27624-27642.
95. Oliveira, M. C.; Ribeiro, R. A. P.; Gracia, L.; de Lazaro, S. R.; de Assis, M.; Oliva, M.; Rosa, I. L. V.; Gurgel, M. F. d. C.; Longo, E.; Andrés, J., Experimental and Theoretical Study of the Energetic, Morphological, and Photoluminescence Properties of $CaZrO_3:Eu^{3+}$. *CrystEngComm* **2018**, *20*, 5519-5530.
96. Silva, G. S.; Gracia, L.; Fabbro, M. T.; Serejo dos Santos, L. P.; Beltrán-Mir, H.; Cordoncillo, E.; Longo, E.; Andrés, J., Theoretical and Experimental Insight on Ag_2CrO_4 Microcrystals: Synthesis, Characterization, and Photoluminescence Properties. *Inorg. Chem.* **2016**, *55*, 8961-8970.
97. http://www.crystal.unito.it/Basis_Sets.
98. Monkhorst, H. J.; Pack, J. D., Special Points for Brillouin-Zone Integrations. *Phys. Rev. B: Condens. Matter.* **1976**, *13*, 5188-5192.
99. Wulff, G., Xxv. Zur Frage Der Geschwindigkeit Des Wachsthums Und Der Auflösung Der Krystallflächen. *Z. Kristallogr. Cryst Mater.* **1901**, *34*, 449-530.
100. Andrés, J.; Gracia, L.; Gouveia, A. F.; Ferrer, M. M.; Longo, E., Effects of Surface Stability on the Morphological Transformation of Metals and Metal Oxides as Investigated by First-Principles Calculations. *Nanotechnology* **2015**, *26*, 405703.
101. Bomio, M. R. D.; Tranquilin, R. L.; Motta, F. V.; Paskocimas, C. A.; Nascimento, R. M.; Gracia, L.; Andres, J.; Longo, E., Toward Understanding the Photocatalytic Activity of $PbMoO_4$ Powders with Predominant (111), (100), (011), and (110) Facets. A Combined Experimental and Theoretical Study. *J. Phys. Chem. C.* **2013**, *117*, 21382-21395.
102. Fabbro, M. T., et al., Synthesis, Antifungal Evaluation and Optical Properties of Silver Molybdate Microcrystals in Different Solvents: A Combined Experimental and Theoretical Study. *Dalton Trans.* **2016**, *45*, 10736-10743.
103. Almeida, C. R. R.; Lovisa, L. X.; Santiago, A. A. G.; Li, M. S.; Longo, E.; Paskocimas, C. A.; Motta, F. V.; Bomio, M. R. D., One-Step Synthesis of $CaMoO_4$: Eu^{3+} Nanospheres by Ultrasonic Spray Pyrolysis *J Mater Sci: Mater Electron.* **2017**, *28*, 16867–16879.
104. Abakumov, A. M.; Morozov, V. A.; Tsirlin, A. A.; Verbeeck, J.; Hadermann, J., Cation Ordering and Flexibility of the BO_4^{2-} Tetrahedra in Incommensurately Modulated $CaEu_2(BO_4)_4$ (B = Mo, W) Scheelites. *Inorg Chem.* **2014**, *53*, 9407-9415.
105. Basiev, T. T.; Sobol, A. A.; Voronko, Y. K.; Zverev, P. G., Spontaneous Raman Spectroscopy of Tungstate and Molybdate Crystals for Raman Lasers. *Opt. Mater.* **2000**, *15*, 205-216.
106. Longo, V. M.; Figueiredo, A. T. d.; Campos, A. B.; Espinosa, J. W. M.; Hernandes, A. C.; Taft, C. A.; Sambrano, J. R.; Varela, J. A.; Longo, E., Different Origins of Green-Light Photoluminescence Emission in Structurally Ordered and Disordered Powders of Calcium Molybdate. *J. Phys. Chem. A.* **2008**, *112*, 8920-8928.
107. Panchal, V.; Garg, N.; Poswal, H. K.; Errandonea, D.; Rodríguez-Hernández, P.; Muñoz, A.; Cavalli, E., High-Pressure Behavior of $CaMoO_4$. *Phys. Rev. Mater.* **2017**, *1*, 043605.

108. Ryu, J. H.; Yoon, J.-W.; Lim, C. S.; Oh, W.-C.; Shim, K. B., Microwave-Assisted Synthesis of $CaMoO_4$ Nano-Powders by a Citrate Complex Method and Its Photoluminescence Property. *J.Alloy.Compd.* **2005**, *390*, 245-249.
109. Bomio, M. R. D.; Cavalcante, L. S.; Almeida, M. A. P.; Tranquilin, R. L.; Batista, N. C.; Pizani, P. S.; Siu Li, M.; Andres, J.; Longo, E., Structural Refinement, Growth Mechanism, Infrared/Raman Spectroscopies and Photoluminescence Properties of $PbMoO_4$ Crystals. *Polyhedron* **2013**, *50*, 532-545.
110. Errandonea, D.; Muñoz, A.; Rodríguez-Hernández, P.; Proctor, J. E.; Sapiña, F.; Bettinelli, M., Theoretical and Experimental Study of the Crystal Structures, Lattice Vibrations, and Band Structures of Monazite-Type $PbCrO_4$, $PbSeO_4$, $SrCrO_4$, and $SrSeO_4$. *Inorg. Chem.* **2015**, *54*, 7524-7535.
111. Botella, P.; Errandonea, D.; Garg, A. B.; Rodriguez-Hernandez, P.; Muñoz, A.; Achary, S. N.; Vomiero, A., High-Pressure Characterization of the Optical and Electronic Properties of $InVO_4$, $InNbO_4$, and $InTaO_4$. *SN Appl. Sci.* **2019**, *1*, 389.
112. Selvalakshmi, T.; Sellaiyan, S.; Uedono, A.; Chandra Bose, A., Investigation of Defect Related Photoluminescence Property of Multicolour Emitting Gd_2O_3:Dy^{3+} Phosphor. *RSC Adv.* **2014**, *4*, 34257-34266.
113. Xie, Y.; Ma, Z.; Liu, L.; Su, Y.; Zhao, H.; Liu, Y.; Zhang, Z.; Duan, H.; Li, J.; Xie, E., Oxygen Defects-Modulated Green Photoluminescence of Tb-Doped ZrO_2 Nanofibers. *Appl. Phys. Lett.* **2010**, *97*, 141916.
114. Tamrakar, R. K.; Bisen, D. P.; Upadhyay, K., Photoluminescence Behavior of ZrO_2: Eu^{3+} with Variable Concentration of Eu^{3+} Doped Phosphor. *J. Radiat. Res. Appl. Sci.* **2015**, *8*, 11-16.
115. Zhang, H. X.; Buddhudu, S.; Kam, C. H.; Zhou, Y.; Lam, Y. L.; Wong, K. S.; Ooi, B. S.; Ng, S. L.; Que, W. X., Luminescence of Eu^{3+} and Tb^{3+} Doped Zn_2SiO_4 Nanometer Powder Phosphors. *Mater. Chem. Phys* **2001**, *68*, 31-35.
116. Muñoz-Santiuste, J. E.; Lavín, V.; Rodríguez-Mendoza, U. R.; Ferrer-Roca, C.; Errandonea, D.; Martínez-García, D.; Rodríguez-Hernández, P.; Muñoz, A.; Bettinelli, M., Experimental and Theoretical Study on the Optical Properties of $LaVO_4$ Crystals under Pressure. *Phys. Chem. Chem. Phys.* **2018**, *20*, 27314-27328.
117. Cheng, Q.; Dong, Y.; Kang, M.; Zhang, P., Preparation and Tunable Luminescence of $CaCO_3$: Eu^{3+}, Tb^{3+} Phosphors. *J. Lumin.* **2014**, *156*, 91-96.
118. Marques, A. P. A.; Motta, F. V.; Cruz, M. A.; Varela, J. A.; Longo, E.; Rosa, I. L. V., $BaMoO_4$:Tb^{3+} Phosphor Properties: Synthesis, Characterization and Photophysical Studies. *Solid State Ionics* **2011**, *202*, 54-59.
119. Parchur, A. K.; Ningthoujam, R. S.; Rai, S. B.; Okram, G. S.; Singh, R. A.; Tyagi, M.; Gadkari, S. C.; Tewari, R.; Vatsa, R. K., Luminescence Properties of Eu^{3+} Doped $CaMoO_4$ Nanoparticles. *Dalton Trans.* **2011**, *40*, 7595-7601.
120. Wang, F.; Liu, X., Recent Advances in the Chemistry of Lanthanide-Doped Upconversion Nanocrystals. *Chem. Soc. Rev.* **2009**, *38*, 976-989.
121. Blasse, G., Energy Transfer in Oxidic Phosphors. *Phys. Lett. A* **1968**, *28*, 444-445.
122. Mukherjee, S.; Dutta, D. P.; Manoj, N.; Tyagi, A. K., Sonochemically Synthesized Rare Earth Double-Doped Zirconia Nanoparticles: Probable Candidate for White Light Emission. *J. Nanopart. Res.* **2012**, *14*, 814.
123. McCamy, C. S., Correlated Color Temperature as an Explicit Function of Chromaticity Coordinates. *Color Res. Appl.* **1992**, *17*, 142-144.
124. Ribeiro, R.A.P; de Lazaro, S. R.; Gracia, L.; Longo, E.; Andrés. J. Theoretical Approach for Determining the Relation between the Morphology and Surface Magnetism of Co_3O_4. *J. Mag. Mag. Mater.* **2018**, *453*, 262.

125. Botelho, G.; Andres, J.; Gracia, L.; Matos, L. S.; Longo, E. Photoluminescence and Photocatalytic Properties of Ag_3PO_4 Microcrystals: An Experimental and Theoretical Investigation. *ChemPlusChem* **2016**, *81*, 202-212.
126. Lai, H.-L.; Yang, R.-Y.; Chang, S.-J., Thermally Stable Luminescence Properties and Energy Transfer of Green-Emitting $LiBaPO_4$: Tb^{3+}, Ce^{3+} Phosphor. *Ceram. Int.* **2017**, *43*, S688-S693.
127. Liu, Y.; Zou, J.; Shi, M.; Yang, B.; Han, Y.; Li, W.; Wang, Z.; Zhou, H.; Li, M.; Jiang, N., Effect of Gallium Ion Content on Thermal Stability and Reliability of Yag: Ce Phosphor Films for White Leds. *Ceram. Int.* **2018**, *44*, 1091-1098.
128. Zhang, Y.; Zhou, T.; Liu, H.; Wang, Y.; Mei, L.; Huang, Z.; Liao, L., Structure and Luminescence Properties of $Sr_9La(PO_4)_5(SiO_4)F_2$:Dy^{3+} Single-Component White-Emitting Phosphor for N-UV W-Leds. *Opt. Mater.* **2018**, *84*, 689-693.

Table Caption

Table 1. $CaMoO_4$: RE^{3+} compositions investigated

Table 2. Values of the chromaticity coordinates (CIE), correlated temperature color (CCT) and color rendering index (CRI) for $CaMoO_4$ and $CaMoO_4$:RE^{3+} samples.

Table 1.

Samples	**RE^{3+}**		
	Eu^{3+} (%)	**Tb^{3+} (%)**	**Tm^{3+} (%)**
$CaMoO_4$	0	0	0
$CaMoO_4$: 1% (RE^{3+})	0.34	0.33	0.33
$CaMoO_4$: 2% (RE^{3+})	0.67	0.67	0.66
$CaMoO_4$: 4% (RE^{3+})	1.34	1.33	1.33

Table 2.

Point Symbol	**Samples**	**CIE (*x*, *y*)**	**CCT (K)**	**CRI**	**Color**
●	$CaMoO_4$	(0.31, 0.41)	6218	91	Yellowish green
■	$CaMoO_4$: 1% (RE/Ca)	(0.39, 0.43)	4105	93	Greenish yellow
▲	$CaMoO_4$: 2% (RE/Ca)	(0.34, 0.34)	5171	95	White
♦	$CaMoO_4$: 4% (RE/Ca)	(0.34, 0.33)	5095	93	White

Figures Caption

Figure 1. Schematic diagram of the experimental apparatus and the formation of $CaMoO_4$ and $CaMoO_4:RE^{3+}$microstructuresobtained by one-pot ultrasonic spray pyrolysis.

Figure 2. XRD patterns $CaMoO_4$ and $CaMoO_4:RE^{3+}$ (x = 1, 2 and 4 mol%) obtained by spray pyrolysis method.

Figure 3. Rietveld refinements of **(a)** $CaMoO_4$, **(b)** $CaMoO_4$: 1% (RE^{3+}), **(c)**$CaMoO_4$: 2% (RE^{3+}), and **(d)** $CaMoO_4$: 4% (RE^{3+})microstructures.

Figure 4. Raman spectra for $CaMoO_4:RE^{3+}$microstructuresmaterials prepared by the pyrolysis spray method.

Figure 5. Theoretical representation of the scheelite type structure tetragonal 2x2x2 supercell corresponding to **(a)** $CaMoO_4$:12.5% mol Eu^{3+}, **(b)** $CaMoO_4$:12.5% mol Tb^{3+} and **(c)** $CaMoO_4$:12.5% mol Tm^{3+} microstructures.

Figure 6. Electronic structure analyzed by band structure and total DOS **(a)** Eu^{3+}, **(b)** $Tb^{3+}$and(**c)** Tm^{3+} ions for $CaMoO_4:RE^{3+}$ (12.5%) 2x2x2 supercell.

Figure 7. UV-visible absorption spectra for particles: **(a)** $CaMoO_4$, **(b)** $CaMoO_4$:1% (RE^{3+}), **(c)** $CaMoO_4$: 2% (RE^{3+}) and **(d)** $CaMoO_4$: 4% (RE^{3+}).

Figure 8.PL emission spectrum of **(a)** $CaMoO_4$ at600 °C, **(b)**deconvolution the PL curve at 600 °C, **(c)** ($CaMoO_4:RE^{3+}$) PL emisisons of the powders obtained at 600 °C by spray pyrolysis method with addition of the RE^{3+}.The characteristic color of each RE^{3+}: Eu^{3+}, Tb^{3+} and Tm^{3+} is depicted.

Figure 9. CIE chromaticity diagram of $CaMoO_4:RE^{3+}$.

Figure 10.FE-SEM images of $CaMoO_4:RE^{3+}$ **(a-b)** undoped, **(c-d)**x: 1%,**(e-f)** x: 2 % and **(g-h)** x: 4%.

Figure 11. (a) Theoretical morphology of pure $CaMoO_4$ and doped 12.5%RE^{3+} **(b)** Available morphologies of $CaMoO_4$: 12.5% Eu^{3+} by tuning the values of E_{surf} of the (100), (001), (112), (110) and (101) exposed surfaces.

Figure 1.

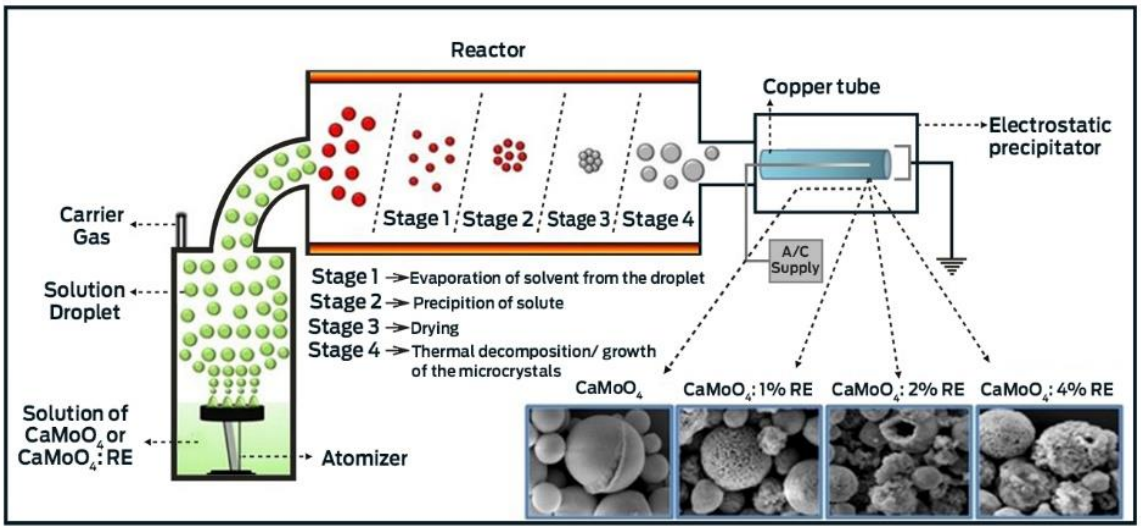
Reactor
Copper tube
Electrostatic precipitator
Carrier Gas
Solution Droplet
Stage 1
Stage 2
Stage 3
Stage 4
A/C Supply
Stage 1 → Evaporation of solvent from the droplet
Stage 2 → Precipition of solute
Stage 3 → Drying
Stage 4 → Thermal decomposition/ growth of the microcrystals
Solution of CaMoO4 or CaMoO4: RE
Atomizer
CaMoO4
CaMoO4: 1% RE
CaMoO4: 2% RE
CaMoO4: 4% RE

Figure 2.

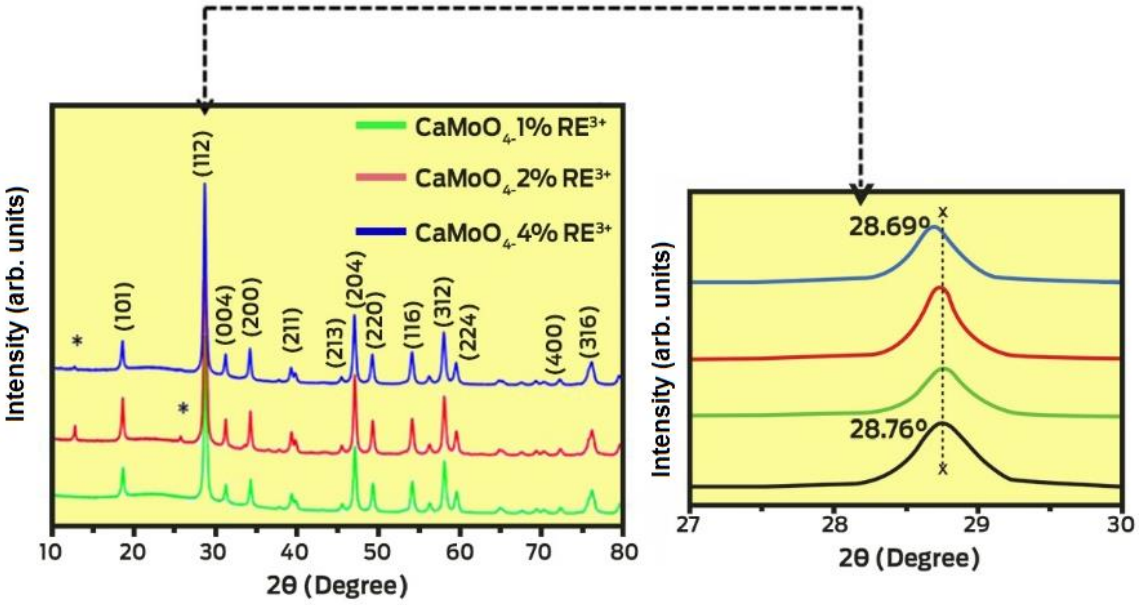
CaMoO4-1% RE3+
CaMoO4-2% RE3+
CaMoO4-4% RE3+
Intensity (arb. units)
2θ (Degree)
(101)
(112)
(004)
(200)
(211)
(213)
(204)
(220)
(116)
(312)
(224)
(400)
(316)
28.69°
28.76°

Figure 3.

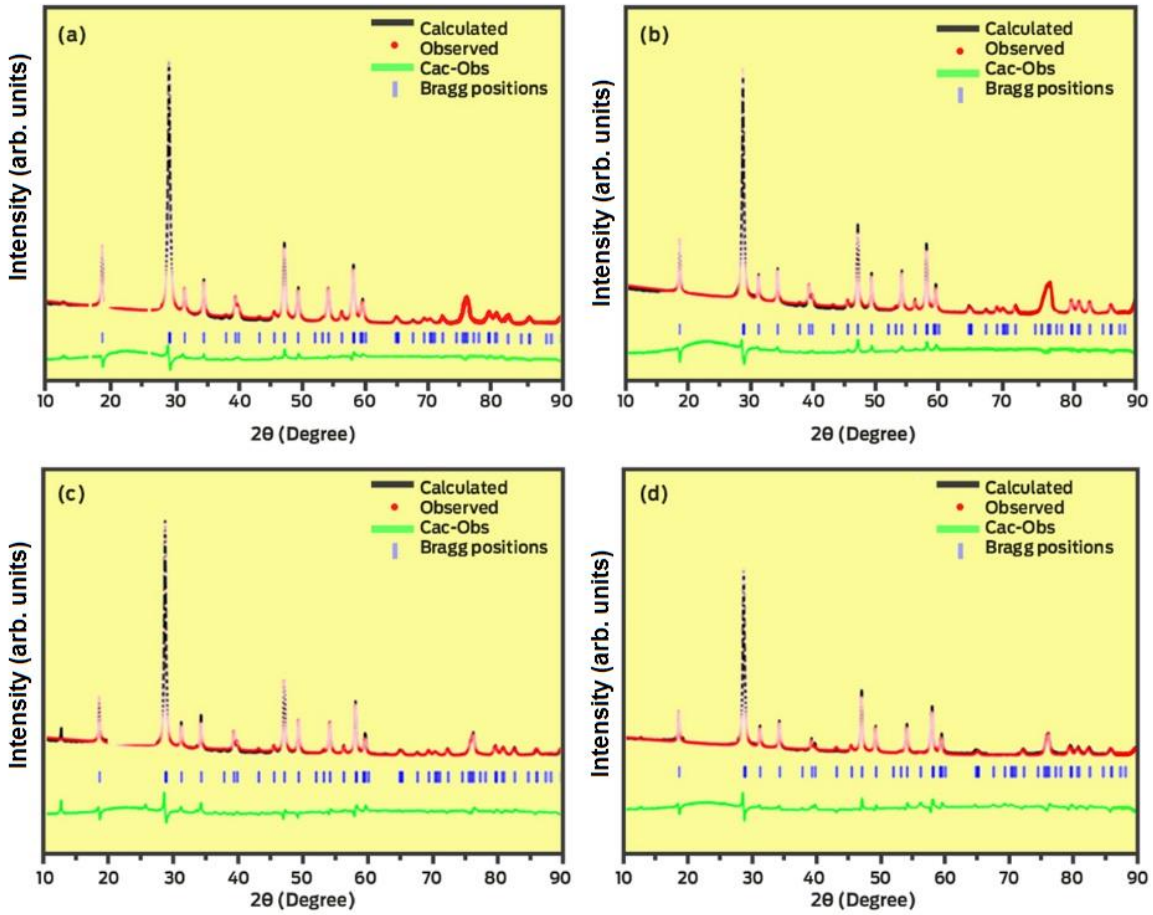
(a)
(b)
(c)
(d)
Calculated
Observed
Cac-Obs
Bragg positions
Intensity (arb. units)
2θ (Degree)
10
20
30
40
50
60
70
80
90

Figure 4.

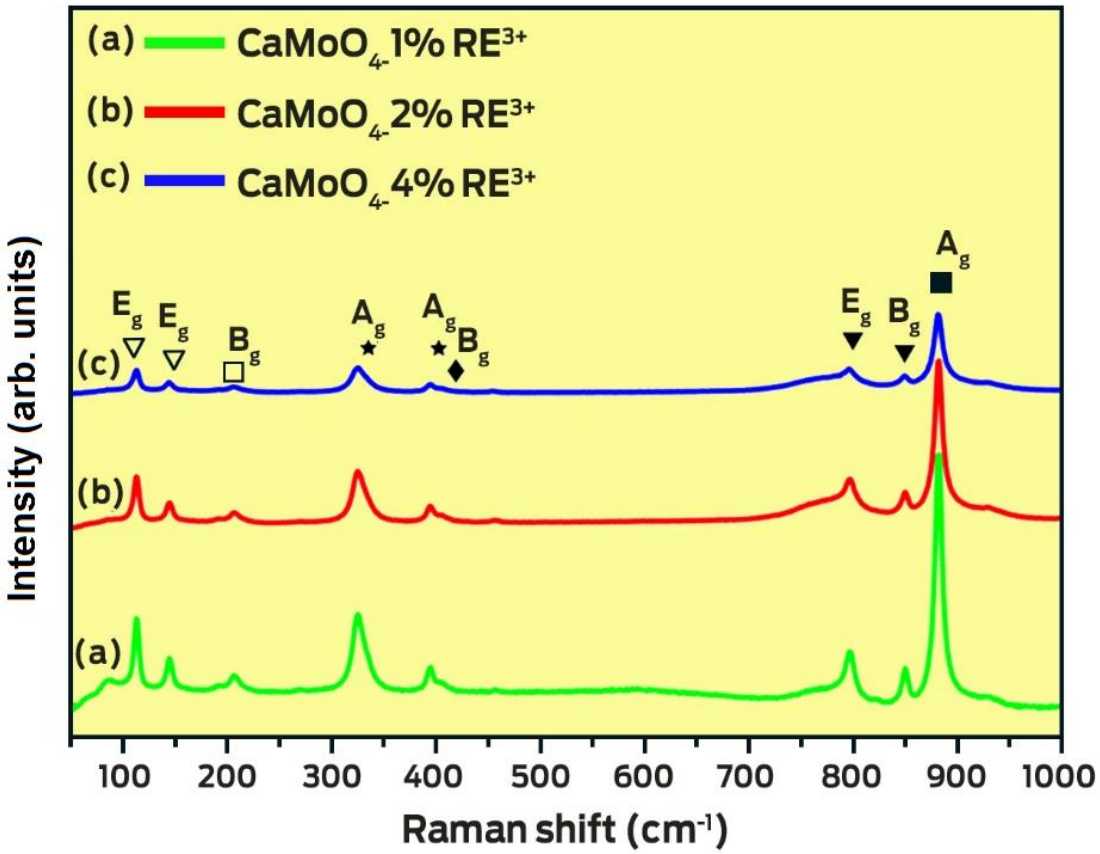
(a) CaMoO4- 1% RE3+
(b) CaMoO4- 2% RE3+
(c) CaMoO4- 4% RE3+
Eg
Eg
Bg
Ag
Ag
Bg
Eg
Bg
Ag
(c)
(b)
(a)
Intensity (arb. units)
100
200
300
400
500
600
700
800
900
1000
Raman shift (cm-1)

Figure 5.

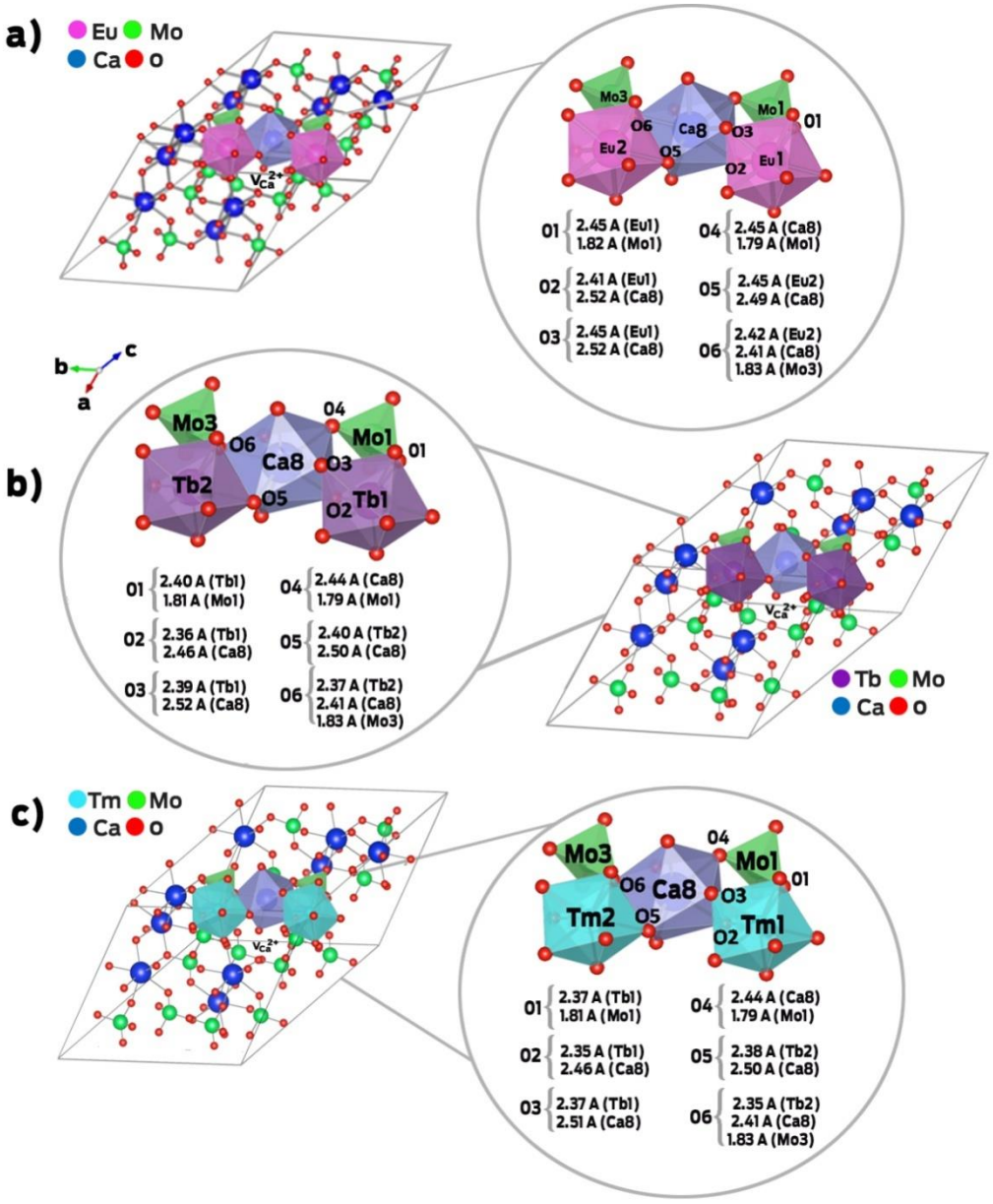
a)
Eu Mo
Ca o
Mo3
O6
Ca8
Mo1
O1
O3
Eu2
O5
O2
Eu1
01 2.45 A (Eu1) 1.82 A (Mo1)
02 2.41 A (Eu1) 2.52 A (Ca8)
03 2.45 A (Eu1) 2.52 A (Ca8)
04 2.45 A (Ca8) 1.79 A (Mo1)
05 2.45 A (Eu2) 2.49 A (Ca8)
06 2.42 A (Eu2) 2.41 A (Ca8) 1.83 A (Mo3)
b)
b
c
a
Mo3
O6
Ca8
04
Mo1
01
O3
Tb2
O5
O2
Tb1
01 2.40 A (Tb1) 1.81 A (Mo1)
02 2.36 A (Tb1) 2.46 A (Ca8)
03 2.39 A (Tb1) 2.52 A (Ca8)
04 2.44 A (Ca8) 1.79 A (Mo1)
05 2.40 A (Tb2) 2.50 A (Ca8)
06 2.37 A (Tb2) 2.41 A (Ca8) 1.83 A (Mo3)
Tb Mo
Ca o
c)
Tm Mo
Ca o
Mo3
04
Mo1
O6
Ca8
01
O3
Tm2
O5
O2
Tm1
01 2.37 A (Tb1) 1.81 A (Mo1)
02 2.35 A (Tb1) 2.46 A (Ca8)
03 2.37 A (Tb1) 2.51 A (Ca8)
04 2.44 A (Ca8) 1.79 A (Mo1)
05 2.38 A (Tb2) 2.50 A (Ca8)
06 2.35 A (Tb2) 2.41 A (Ca8) 1.83 A (Mo3)

Figure 6.

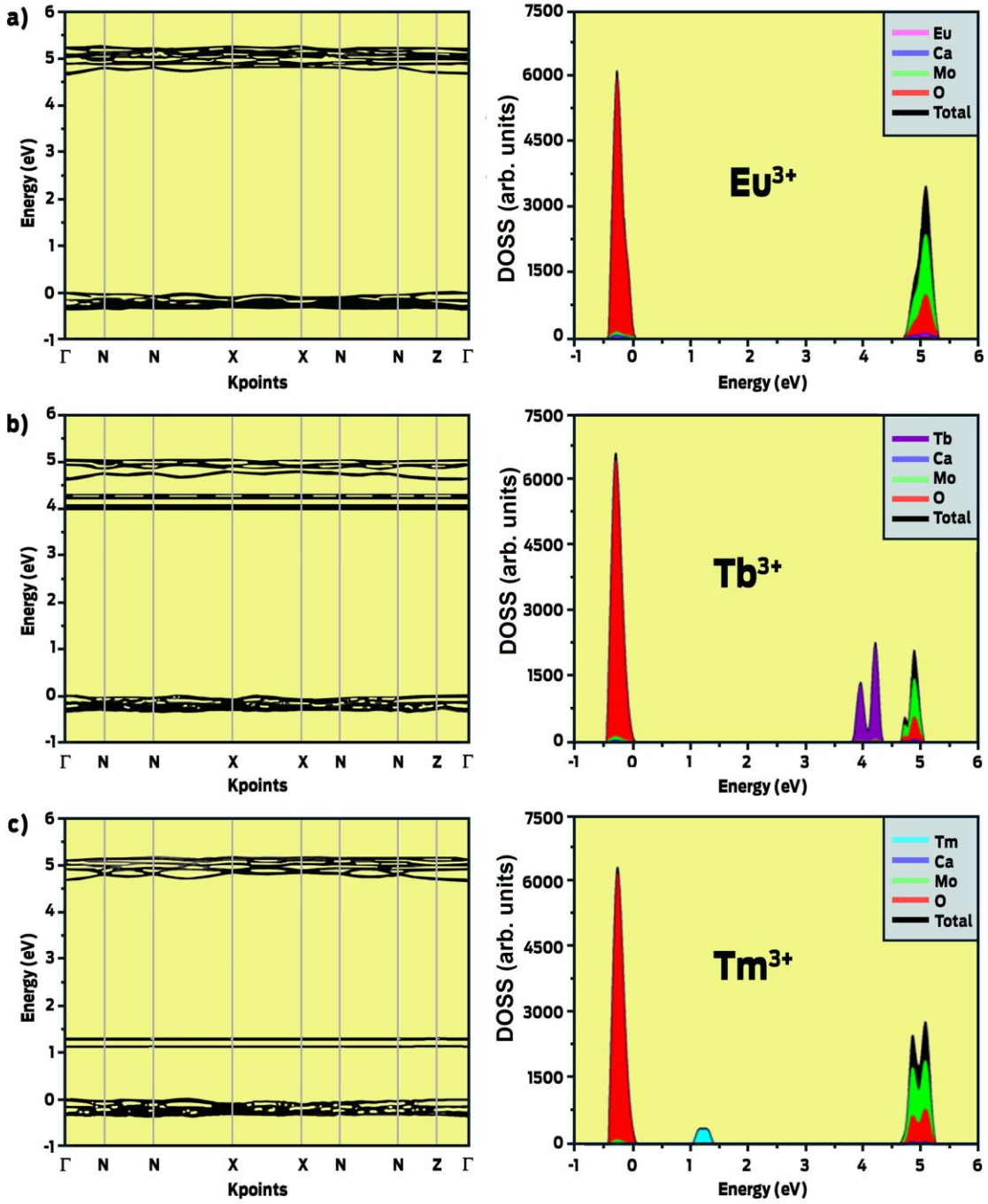
a)
Energy (eV)
Kpoints
Γ N N X X N N Z Γ
DOSS (arb. units)
Energy (eV)
Eu
Ca
Mo
O
Total
Eu3+
b)
Energy (eV)
Kpoints
Γ N N X X N N Z Γ
DOSS (arb. units)
Energy (eV)
Tb
Ca
Mo
O
Total
Tb3+
c)
Energy (eV)
Kpoints
Γ N N X X N N Z Γ
DOSS (arb. units)
Energy (eV)
Tm
Ca
Mo
O
Total
Tm3+

Figure 7.

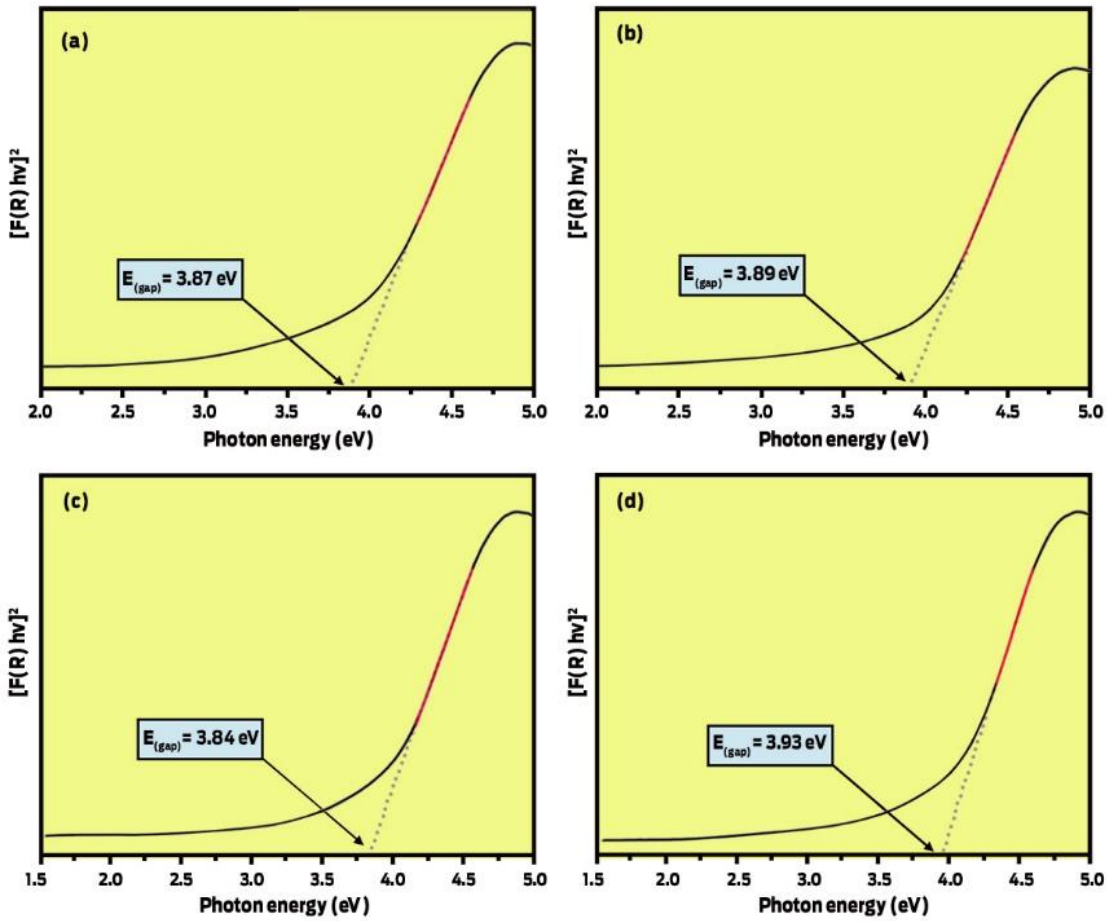
(a)
[F(R) hν]²
E(gap) = 3.87 eV
2.0 2.5 3.0 3.5 4.0 4.5 5.0
Photon energy (eV)
(b)
[F(R) hν]²
E(gap) = 3.89 eV
2.0 2.5 3.0 3.5 4.0 4.5 5.0
Photon energy (eV)
(c)
[F(R) hν]²
E(gap) = 3.84 eV
1.5 2.0 2.5 3.0 3.5 4.0 4.5 5.0
Photon energy (eV)
(d)
[F(R) hν]²
E(gap) = 3.93 eV
1.5 2.0 2.5 3.0 3.5 4.0 4.5 5.0
Photon energy (eV)

Figure 8.

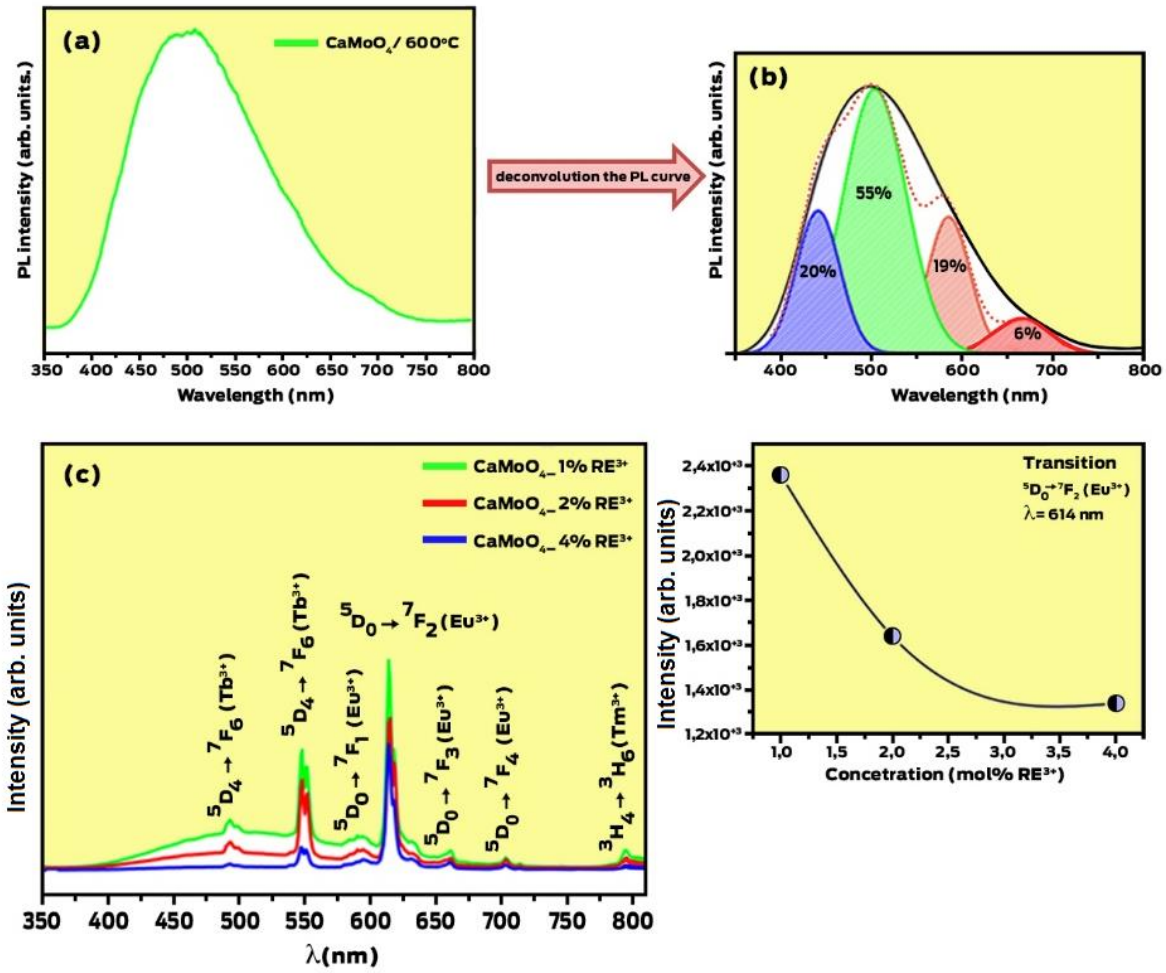
(a)
CaMoO4 / 600°C
PL intensity (arb. units.)
Wavelength (nm)
deconvolution the PL curve
(b)
55%
20%
19%
6%
(c)
CaMoO4 – 1% RE3+
CaMoO4 – 2% RE3+
CaMoO4 – 4% RE3+
Intensity (arb. units)
λ(nm)
Transition
λ= 614 nm
Concetration (mol% RE3+)

Figure 9.

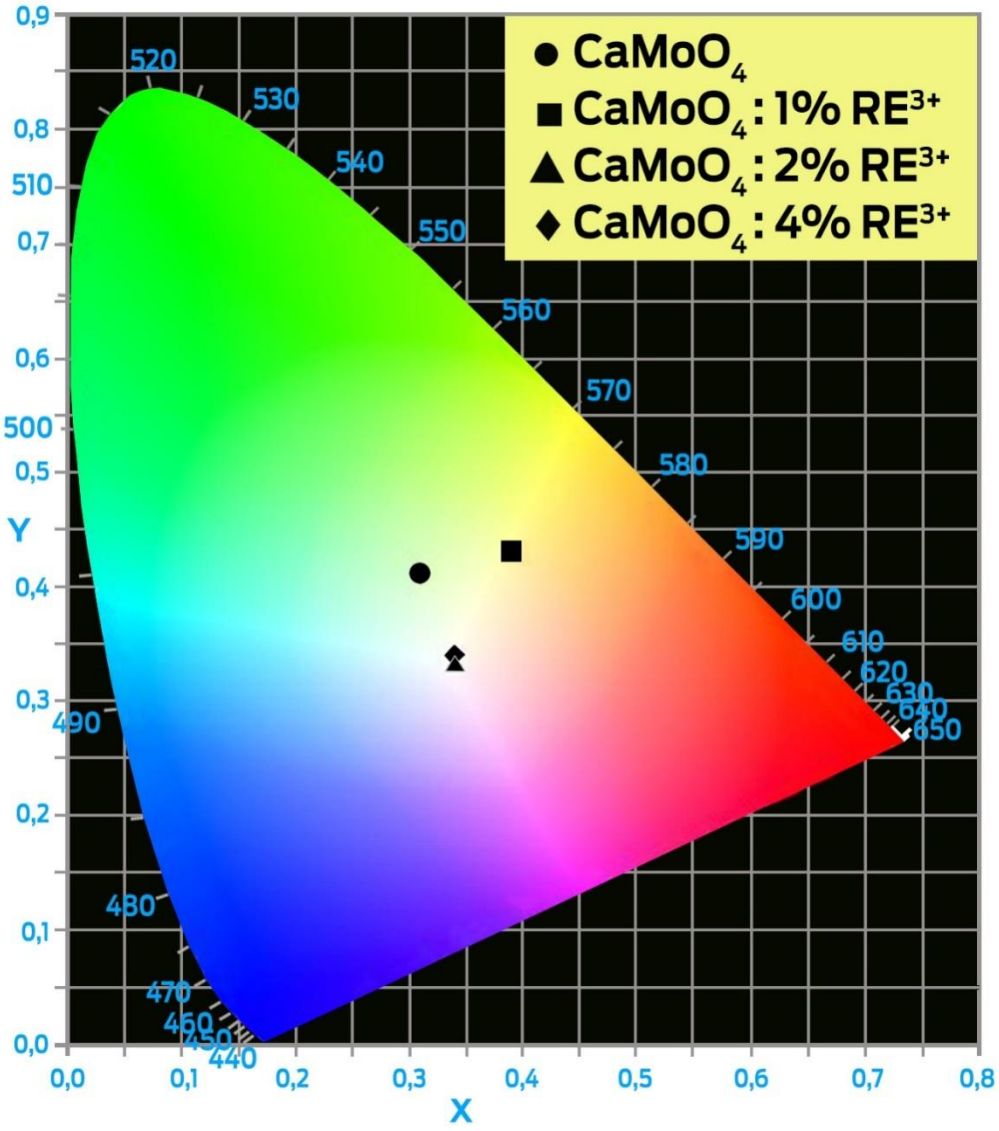
● CaMoO4
■ CaMoO4 : 1% RE3+
▲ CaMoO4 : 2% RE3+
♦ CaMoO4 : 4% RE3+
Y
X
0,0
0,1
0,2
0,3
0,4
0,5
0,6
0,7
0,8
0,9
490
500
510
520
530
540
550
560
570
580
590
600
610
620
630
640
650
480
470
460
450
440

Figure 10.

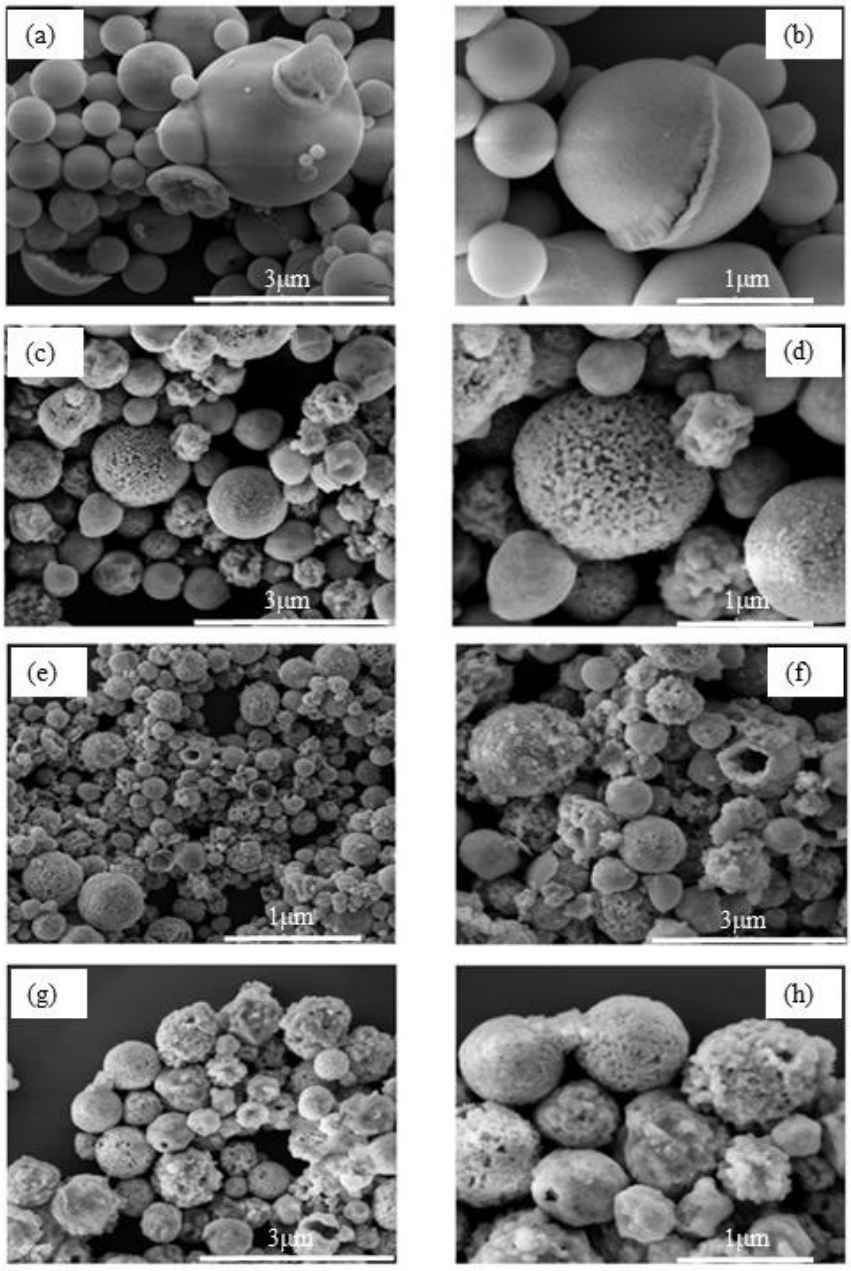

Figure 11.

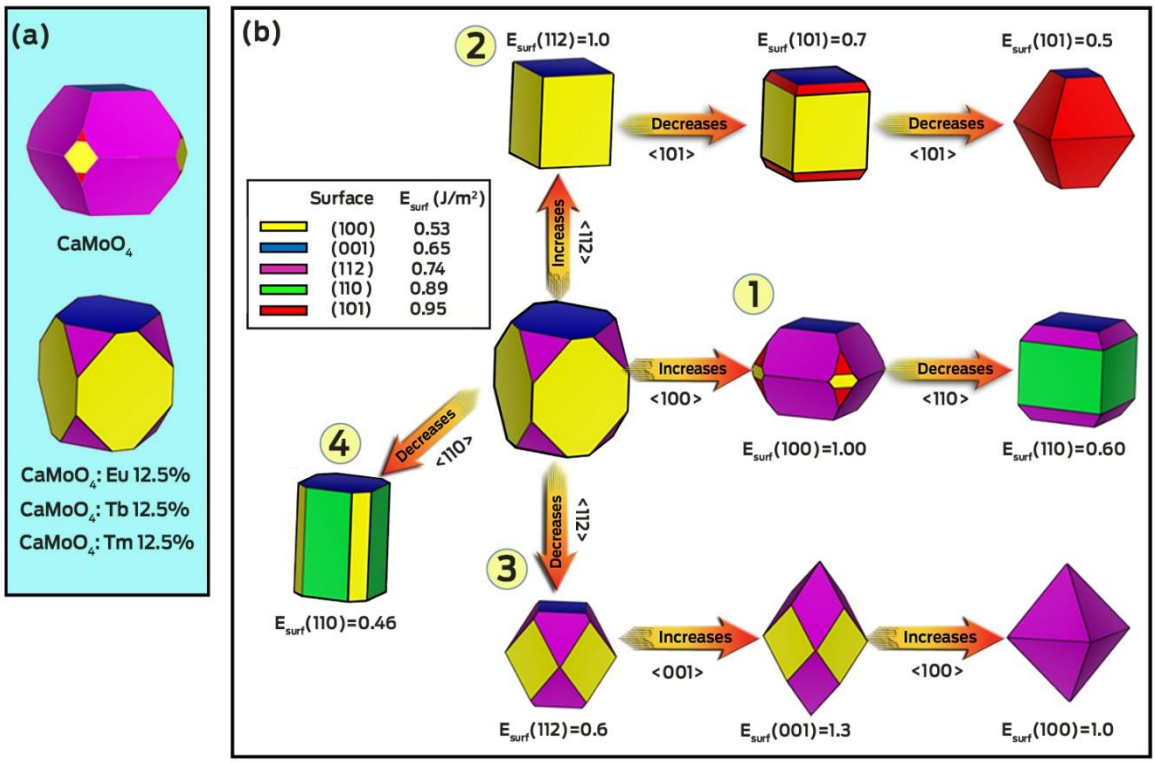
(a)
CaMoO4
CaMoO4: Eu 12.5%
CaMoO4: Tb 12.5%
CaMoO4: Tm 12.5%
(b)
Surface Esurf (J/m²)
(100) 0.53
(001) 0.65
(112) 0.74
(110) 0.89
(101) 0.95
1
2
3
4
Esurf(112)=1.0
Esurf(101)=0.7
Esurf(101)=0.5
Esurf(100)=1.00
Esurf(110)=0.60
Esurf(110)=0.46
Esurf(112)=0.6
Esurf(001)=1.3
Esurf(100)=1.0
Decreases <101>
Decreases <101>
Increases <112>
Increases <100>
Decreases <110>
Decreases <110>
Decreases <112>
Increases <001>
Increases <100>

Synopsis

Spray pyrolysis synthesis of $CaMoO_4$ and rare earth cation (RE^{3+})-doped $CaMoO_4$:RE^{3+} microstructures (RE^{3+} = Eu^{3+}, Tb^{3+}, and Tm^{3+};and x=1%, 2%, and 4% mol)and theoretical method based on the calculations of surface energies and Wulff construction were applied to evaluate the transformation of the $CaMoO_4$ and $CaMoO_4$:RE^{3+}microstructures with respect to their shapes. The PL emissions revealed the presence of a new white light emitter (samples doped with 2% and 4% of RE^{3+}) display white emissions.

TOC graphic

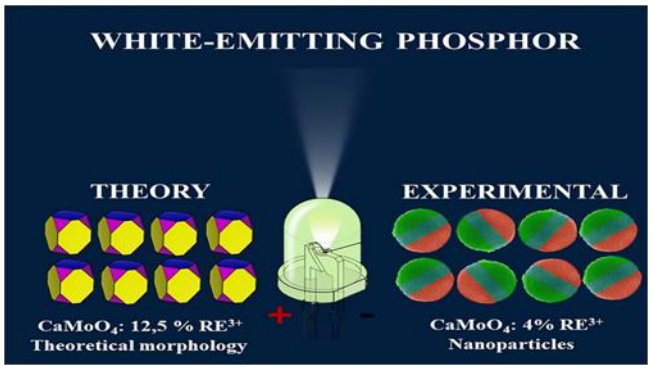

Understanding the White-Emitting $CaMoO_4$ Co-Doped Eu^{3+}, Tb^{3+} and Tm^{3+} Phosphor Through Experiment and Computation

R.L. Tranquilin[a], L.X. Lovisa[a], C.R.R. Almeida[a], C.A. Paskocimas[a], M.S. Li[b], M. C. Oliveira[a,c], L. Gracia[c,#], J.Andres[c], E. Longo[d,*], F.V. Motta[a], M.R.D. Bomio[a]

[a]LSQM – Laboratory of Chemical Synthesis of Materials – Department of Materials Engineering, Federal University of Rio Grande do Norte, P.O. Box 1524, 59078-900, Natal, RN, Brazil.

[b] IFSC, USP, Av. Trabalhador São Carlense, 400, CEP 13566-590, São Carlos, SP, Brazil

[c]Departament de Química Física i Analítica, Universitat Jaume I, 12071 Castelló de la Plana, Spain

[#] Permanent address: Department of Physical Chemistry, Universitat de València, 46100 Burjassot, Spain

[d] CDMF-LIEC, UFSCar, P.O. Box 676, 13565-905 São Carlos, SP, Brazil

Supplementary Information

Table S1: Rietveld refined structural parameters for $CaMoO_4$ and $CaMoO_4$:RE (x= 1, 2 and 4 mol%) nanoparticles with the space group symmetry I41/a.

Compounds	**$CaMoO_4$**	**$CaMoO_4$: 1%RE^{3+}**	**$CaMoO_4$: 2%RE^{3+}**	**$CaMoO_4$: 4%RE^{3+}**	**ICSD 60552**
a = b (Å)	5.2241	5.2248	5.2288	5.2356	5.1286
c (Å)	11.4400	11.4341	11.4396	11.4460	11.119
c/a	2.1898	2.1884	2.1878	2.1861	2.1680
V $(Å)^3$	312.2115	312.1341	312.7626	313.7521	292.4579
D (nm)	31.53	38.54	44.73	40.41	
Ɛ (x10 $^{-4}$)	17.75	6.87	10.08	12.82	
X^2	1.41	1.23	1.73	1.12	
Rw	2.06	2.57	2.91	1.59	
Rb	1.94	2.13	2.25	1.24	
Rwnb	1.98	2.44	3.05	1.53	
Rexp	1.46	2.08	1.68	1.41	

Table S2: Calculated B3LYP values of the atomics coordinates in Cartesian coordinates (Å) for the $CaMoO_4$ doped with Eu^{3+}, Tb^{3+} and Tm^{3+} using a supercell 2x2x2.

	Cartesian Coordinates				Cartesian Coordinates				Cartesian Coordinates		
Atom	X	Y	Z	Atom	X	Y	Z	Atom	X	Y	Z
EU	0.014	0.007	0.006	O	-3.443	-1.351	12.326	O	-4.385	1.351	1.812
CA	2.629	2.633	-5.679	O	-0.827	1.303	6.648	O	1.351	1.809	-0.982
EU	2.628	-2.625	5.691	O	-5.988	1.131	6.758	O	-1.301	-0.813	4.720
CA	5.263	-0.003	-0.005	O	-3.450	3.903	0.963	O	-1.305	4.404	-6.663
CA	-2.632	2.625	5.674	O	-0.818	-3.940	6.634	O	-3.881	1.807	-0.973
CA	-0.010	5.247	-0.012	O	1.815	-1.337	0.974	O	3.945	-0.799	-6.618
CA	-0.015	-0.004	11.371	O	-3.422	-1.367	0.976	O	1.354	-3.428	-0.966
CA	0.017	2.645	-2.861	O	-0.815	1.307	-4.729	O	1.335	1.814	-12.314
CA	-2.647	0.019	2.872	O	3.902	0.800	-1.879	O	-1.134	-0.749	-6.751
CA	2.647	0.079	2.890	O	1.308	-1.835	3.778	O	-1.361	-1.822	10.388
CA	-0.013	-2.612	8.514	O	1.260	3.443	-7.564	O	1.133	0.741	4.612
CA	2.620	-0.012	-8.501	O	-1.319	0.840	-1.840	O	-3.939	0.807	4.748
CA	-0.047	-2.641	-2.898	O	1.145	3.477	3.761	O	-1.368	3.435	-0.961
CA	5.291	-2.636	-2.887	O	-1.343	0.806	9.514	O	1.308	-4.413	4.705
CA	2.630	-5.330	2.879	O	-1.385	6.073	-1.821	O	3.894	-1.823	-0.980
MO	2.634	2.631	0.006	O	-3.918	3.422	3.776	O	-1.320	-1.805	-0.955
MO	-0.029	0.008	5.690	O	1.324	-0.818	-1.861	O	1.304	0.821	-6.643
MO	0.011	5.235	-5.695	O	-1.254	-3.434	3.805				
MO	-2.635	2.629	0.011	O	-1.309	1.825	-7.586				
MO	5.243	0.016	-5.686	O	-3.866	-0.826	-1.827				
MO	2.632	-2.631	-0.006	O	-1.333	1.836	3.777				
MO	2.622	2.616	-11.373	O	-3.901	-0.805	9.495				
MO	0.030	-0.006	-5.681	O	-3.913	4.408	-1.828				
MO	2.620	-0.004	-2.837	O	-6.393	1.759	3.756				
MO	0.011	-2.639	2.833	O	1.817	1.264	-3.812				
MO	-0.009	2.635	-8.534	O	-0.806	-1.337	1.879				
MO	-2.626	0.025	-2.810	O	-0.802	3.902	-9.519				
MO	-0.049	2.626	2.809	O	-3.432	1.335	-3.772				
MO	-2.616	0.011	8.535	O	-0.856	3.901	1.825				
MO	-2.633	5.214	-2.801	O	-3.408	1.294	7.586				
MO	-5.203	2.626	2.802	O	-3.475	6.416	-3.750				
O	3.442	1.345	0.947	O	-6.076	3.876	1.830				
O	0.817	-1.313	6.631	O	3.404	-1.281	-3.786				
O	0.821	3.947	-4.736	O	0.798	-3.907	1.857				
O	-1.787	1.335	0.970	O	0.796	1.355	-9.487				
O	5.980	-1.133	-4.594	O	-1.790	-1.177	-3.756				
O	3.420	-3.902	0.969	O	0.834	1.350	1.836				
O	3.421	1.368	-10.376	O	-1.807	-1.257	7.554				
O	0.821	-1.295	-4.711	O	-1.819	3.904	-3.769				

Atom	Cartesian Coordinates X	Y	Z	Atom	Cartesian Coordinates X	Y	Z	Atom	Cartesian Coordinates X	Y	Z
TB	0.007	0.000	0.004	O	1.778	-1.300	0.949	O	1.131	0.746	4.577
CA	2.621	2.623	-5.650	O	-3.403	-1.362	0.971	O	-3.938	0.804	4.707
TB	2.620	-2.618	5.664	O	-0.840	1.332	-4.722	O	-1.366	3.428	-0.967
CA	5.250	-0.005	-0.005	O	3.876	0.796	-1.860	O	1.341	-4.380	4.715
CA	-2.621	2.621	5.645	O	1.326	-1.841	3.796	O	3.882	-1.816	-0.964
CA	-0.014	5.238	-0.014	O	1.240	3.435	-7.516	O	-1.278	-1.774	-0.917
CA	-0.019	-0.004	11.312	O	-1.296	0.818	-1.800	O	1.300	0.820	-6.601
CA	0.010	2.638	-2.846	O	1.152	3.466	3.734				
CA	-2.638	0.018	2.851	O	-1.342	0.806	9.471				
CA	2.639	0.079	2.873	O	-1.385	6.062	-1.821				
CA	-0.014	-2.607	8.457	O	-3.906	3.415	3.765				
CA	2.616	-0.014	-8.457	O	1.300	-0.805	-1.801				
CA	-0.048	-2.636	-2.877	O	-1.244	-3.412	3.776				
CA	5.280	-2.632	-2.874	O	-1.324	1.829	-7.485				
CA	2.623	-5.314	2.875	O	-3.842	-0.816	-1.819				
MO	2.613	2.617	0.001	O	-1.325	1.827	3.746				
MO	-0.019	0.000	5.660	O	-3.895	-0.811	9.446				
MO	-0.006	5.220	-5.674	O	-3.904	4.399	-1.840				
MO	-2.622	2.612	0.010	O	-6.372	1.736	3.749				
MO	5.248	0.015	-5.662	O	1.796	1.259	-3.782				
MO	2.618	-2.612	0.016	O	-0.770	-1.292	1.846				
MO	2.628	2.614	-11.325	O	-0.817	3.885	-9.458				
MO	0.024	0.004	-5.632	O	-3.394	1.353	-3.789				
MO	2.590	-0.014	-2.805	O	-0.855	3.879	1.800				
MO	0.021	-2.599	2.821	O	-3.405	1.291	7.546				
MO	-0.032	2.616	-8.467	O	-3.472	6.389	-3.763				
MO	-2.608	0.046	-2.799	O	-6.064	3.864	1.832				
MO	-0.038	2.607	2.778	O	3.390	-1.285	-3.752				
MO	-2.609	0.007	8.488	O	0.800	-3.872	1.849				
MO	-2.622	5.193	-2.815	O	0.779	1.340	-9.420				
MO	-5.187	2.613	2.794	O	-1.772	-1.159	-3.739				
O	3.434	1.341	0.946	O	0.820	1.332	1.781				
O	0.842	-1.337	6.558	O	-1.795	-1.253	7.501				
O	0.811	3.940	-4.712	O	-1.829	3.880	-3.800				
O	-1.756	1.304	0.929	O	-4.364	1.351	1.790				
O	5.976	-1.135	-4.567	O	1.318	1.775	-0.951				
O	3.409	-3.882	0.994	O	-1.289	-0.815	4.682				
O	3.412	1.366	-10.320	O	-1.337	4.365	-6.595				
O	0.824	-1.280	-4.658	O	-3.864	1.797	-0.986				
O	-3.440	-1.342	12.260	O	3.949	-0.795	-6.600				
O	-0.827	1.289	6.621	O	1.351	-3.418	-0.951				
O	-5.986	1.134	6.722	O	1.336	1.811	-12.262				
O	-3.444	3.888	0.959	O	-1.131	-0.753	-6.700				

O	-0.809	-3.929	6.595	O	-1.367	-1.820	10.320					

	Cartesian Coordinates				Cartesian Coordinates				Cartesian Coordinates			
Atom	**X**	**Y**	**Z**	**Atom**	**X**	**Y**	**Z**	**Atom**	**X**	**Y**	**Z**
TM	0.008	0.009	0.005	O	1.768	-1.288	0.943	O	1.127	0.751	4.562
CA	2.618	2.621	-5.640	O	-3.408	-1.366	0.971	O	-3.939	0.801	4.699
TM	2.616	-2.615	5.651	O	-0.847	1.344	-4.722	O	-1.366	3.426	-0.973
CA	5.243	-0.007	-0.005	O	3.866	0.799	-1.856	O	1.351	-4.369	4.718
CA	-2.621	2.620	5.640	O	1.322	-1.842	3.797	O	3.880	-1.815	-0.962
CA	-0.013	5.236	-0.012	O	1.233	3.429	-7.502	O	-1.270	-1.763	-0.911
CA	-0.015	-0.004	11.295	O	-1.295	0.820	-1.792	O	1.298	0.818	-6.590
CA	0.007	2.634	-2.843	O	1.154	3.465	3.730				
CA	-2.636	0.015	2.843	O	-1.337	0.806	9.457				
CA	2.634	0.072	2.868	O	-1.379	6.061	-1.821				
CA	-0.010	-2.603	8.441	O	-3.902	3.412	3.763				
CA	2.616	-0.017	-8.444	O	1.302	-0.797	-1.785				
CA	-0.045	-2.629	-2.866	O	-1.242	-3.412	3.772				
CA	5.278	-2.634	-2.870	O	-1.325	1.828	-7.461				
CA	2.622	-5.309	2.874	O	-3.839	-0.814	-1.818				
MO	2.604	2.613	-0.001	O	-1.329	1.828	3.738				
MO	-0.017	-0.004	5.647	O	-3.887	-0.814	9.437				
MO	-0.013	5.216	-5.664	O	-3.900	4.399	-1.842				
MO	-2.616	2.605	0.007	O	-6.368	1.730	3.744				
MO	5.249	0.016	-5.652	O	1.789	1.259	-3.776				
MO	2.614	-2.605	0.019	O	-0.771	-1.294	1.830				
MO	2.632	2.614	-11.308	O	-0.824	3.879	-9.441				
MO	0.021	0.008	-5.618	O	-3.389	1.357	-3.792				
MO	2.585	-0.016	-2.801	O	-0.853	3.872	1.793				
MO	0.019	-2.593	2.815	O	-3.402	1.291	7.539				
MO	-0.037	2.608	-8.453	O	-3.467	6.385	-3.765				
MO	-2.606	0.054	-2.796	O	-6.054	3.863	1.831				
MO	-0.037	2.604	2.775	O	3.387	-1.290	-3.743				
MO	-2.604	0.006	8.476	O	0.804	-3.866	1.848				
MO	-2.615	5.192	-2.816	O	0.777	1.331	-9.403				
MO	-5.182	2.610	2.792	O	-1.766	-1.149	-3.736				
O	3.428	1.341	0.945	O	0.811	1.325	1.774				
O	0.848	-1.344	6.536	O	-1.788	-1.253	7.487				
O	0.811	3.940	-4.700	O	-1.830	3.879	-3.805				
O	-1.749	1.290	0.916	O	-4.357	1.350	1.785				
O	5.975	-1.136	-4.557	O	1.297	1.769	-0.936				
O	3.407	-3.874	0.999	O	-1.288	-0.817	4.667				
O	3.412	1.363	-10.305	O	-1.350	4.356	-6.574				
O	0.827	-1.272	-4.640	O	-3.863	1.796	-0.989				
O	-3.436	-1.341	12.247	O	3.953	-0.797	-6.592				

O	-0.826	1.283	6.610	O	1.353	-3.417	-0.950	
O	-5.981	1.139	6.714	O	1.344	1.808	-12.248	
O	-3.436	3.880	0.957	O	-1.127	-0.759	-6.687	
O	-0.812	-3.930	6.589	O	-1.371	-1.820	10.302	

Table S3: E_{surf} values of the $CaMoO_4$ doped with Eu^{3+}, Tb^{3+} and Tm^{3+} obtained by calculations using a supercell 2x2.

Surface	**E_{surf} (J/m^2)**		
	Eu (12.5%)	**Tb (12.5%)**	**Tm (12.5%)**
(100)	0.53	0.53	0.50
(001)	0.65	0.65	0.60
(112)	0.74	0.77	0.72
(110)	0.89	0.94	0.87
(101)	0.95	0.99	0.91

Figure S1. First Brillouin zone of scheelite **(MEJORAR)**. A schematic representation of band structure and total DOS calculated for the $CaMoO_4$ **(a)** Eu^{3+}, **(b)** Tb^{3+} and **(c)** Tm^{3+}) ions.

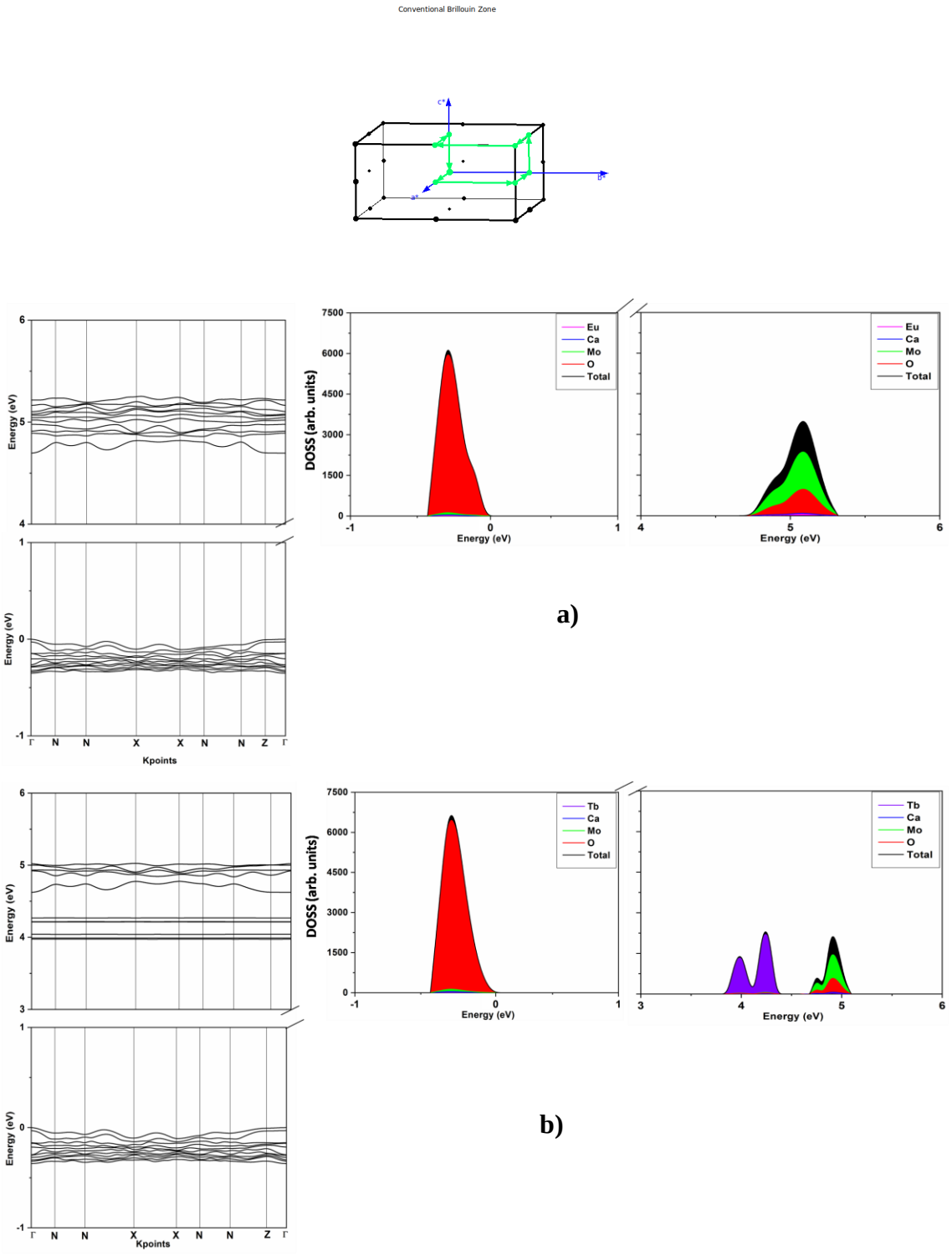

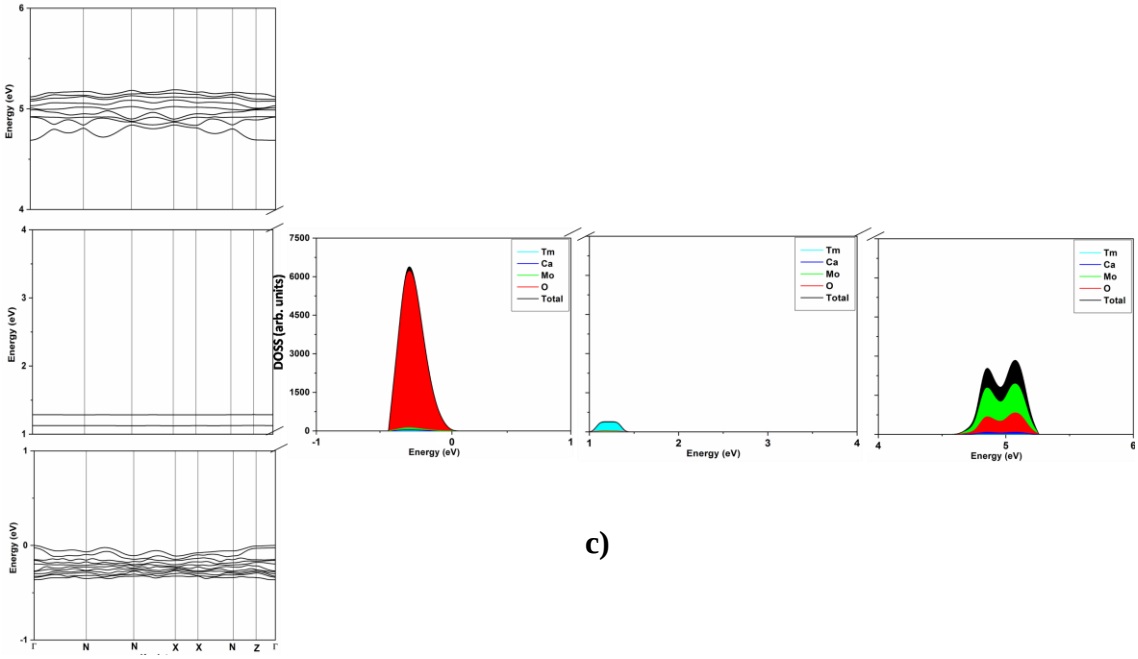

c)

Figure S2. The studied surfaces of $CaMoO_4$:RE^{3+} systems (RE^{3+} = Eu^{3+}, Tb^{3+}, and Tm^{3+})

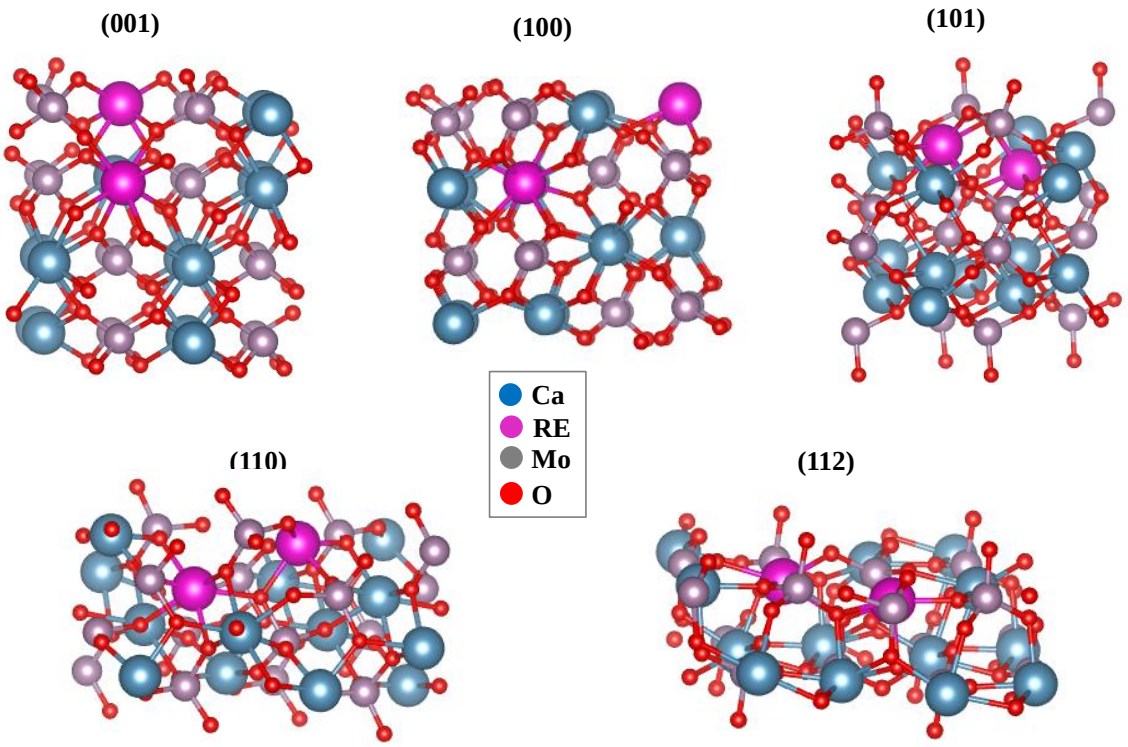

Figure S3. (a) EDS spectrum; **(b)** Mapping of the atom distributions.